J Electroceram (2010) 24:177–199
DOI 10.1007/s10832-008-9554-7

FEATURE ARTICLE

Novel deposition techniques for metal oxide: Prospects for gas sensing

K. Sahner · H. L. Tuller

Received: 28 April 2008 / Accepted: 25 September 2008 / Published online: 16 October 2008

Abstract With the growing need for high performance gas sensors, a variety of preparation methods have been introduced and investigated. In the present contribution, the focus is on novel means for preparing metal oxide gas sensor devices. First, the key gas sensor concepts are reviewed as well as the conventional deposition techniques widely used for thick and thin film deposition of metal oxides such as screen-printing and chemical and physical vapour deposition. This is followed by a review and examination of innovative deposition techniques developed within the past several years, focusing on methods with direct-write features as well as techniques offering precise control of micro- and nano-structural features of the deposited materials.

Keywords Metal oxide · Gas sensor · Electrodeposition · Nanowires · Thin films

1 Introduction

Due to increasingly stringent environmental and safety regulations, reliable detection of hazardous, harmful, or toxic gases has become ever more important. As a consequence, the design of reproducible gas sensor devices with enhanced features has become a highly active research field.

K. Sahner · H. L. Tuller
Department of Materials Science and Engineering,
Massachusetts Institute of Technology,
Cambridge, MA 02139, USA

K. Sahner (✉)
Functional Materials Laboratory, University of Bayreuth,
95440 Bayreuth, Germany
e-mail: kcsahner@mit.edu

Besides exhibiting rapid, reversible, and reproducible response, a gas sensor should meet the following requirements.

- High sensitivity, i.e., a pronounced signal even in the presence of a small concentration of a specific target gas.
- High selectivity towards the target gas.
- Stability, both chemical and mechanical, for extended periods, often in harsh environments such as an automobile exhaust.
- Low cost to manufacture.

Metal oxide gas sensors offer the potential for accessing applications where the use of conventional analytical systems such as gas chromatography (GC) or optical detection (e.g. by infrared radiation) is prohibitively expensive. The interaction between the analyte in the surrounding gas phase and the metal oxide is detected either as a change in electrical conductance, capacitance, or potential of the active element. During the past several decades, a multitude of simple, robust, solid-state metal oxide sensors have been designed [1]. At the same time, mechanistic models were developed to better understand the processes involved in gas sensing, and to identify parameters that offer means for optimizing sensor performance.

The development of models revealing the parameters responsible for gas sensitivity provided an incentive for the investigation of novel deposition methods, allowing for precise nanoscale structuring of specimens. Novel nanostructures such as nanofibers and nanorods, as well as films with tailored porosity, have received particular attention. In addition, progress in many direct-write technologies including ink-jet printing, robocasting, microdispensing, and laser assisted patterning offer opportunities for preparing functional structures with controlled microstructure and the advantage of direct patterning without need for masks.

This feature article is organized as follows. First, metal oxide gas sensors are briefly reviewed with emphasis on the

present understanding of the underlying operating mechanisms and the need for films and other structures with well-defined morphology. This section, with particular focus on semiconducting sensors of the conductometric (or Taguchi) type, is followed by an overview of the state-of-the-art of deposition techniques utilized in sensor fabrication. Then, Section 4 reviews recently reported deposition techniques that show promise in gas sensor technology.

2 Metal oxide gas sensors

Figure 1 presents an overview of the 340 papers dealing with metal oxide gas sensors published in sensor-related journals (listed in the ISI Web of Science database) in 2007. The large number of publications attests to the strong continued interest in this technology. The review of metal oxide gas sensors presented in this section focuses on the four main groups identified in Fig. 1. These include conductometric sensors relying on conductance or resistance changes, potentiometric or amperometric devices utilizing solid-state electrochemical cells, semiconducting metal oxide field effect transistors (MOSFET), and mass sensitive devices based on bulk or surface acoustic waves. Other devices, such as thermoelectric sensors [2–4] or optical evanescent field devices [5, 6] are beyond the scope of this review and are not included here.

2.1 Resistive or conductometric type

Metal oxide semiconducting sensors of the resistive or conductometric type have been investigated for decades. This group can be divided into two major subgroups, i.e., "bulk" or "surface exchange" type, depending on where the sensing effect occurs.

In the case of bulk type sensors, the internal defect equilibrium within the metal oxide is affected by the surrounding gas. The classic example is the bulk reduction/

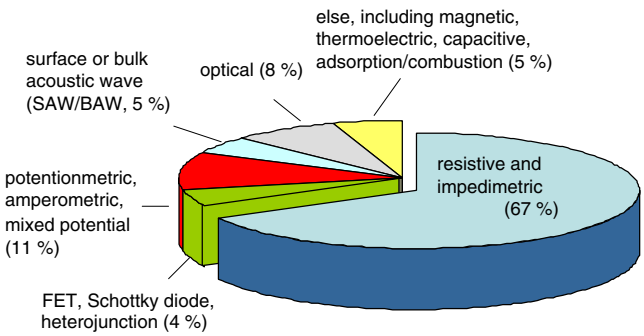

Fig. 1 Literature review: various types of metal oxide based gas sensors discussed in 2007 (based on a total of 340 papers available via Isi Web of Science). For details on the respective sensor mechanisms see text

oxidation reaction of *n*-type semiconducting metal oxides with oxygen in the gas phase according to

$$^1/_2O_2 + V_o^{\cdot\cdot} + e' \Leftrightarrow O_o^x \quad (1)$$

during which doubly ionized oxygen vacancies $V_o^{\cdot\cdot}$ in the oxygen ion sublattice O_o^x are filled with oxygen ions stemming from the surrounding atmosphere with oxygen partial pressure pO_2. Since electrons e′ are either consumed (oxidation) or generated (reduction) during the reaction, this results in a corresponding decrease or increase in the conductivity σ of the material.[1] Relationships between σ and pO_2 of the form $\sigma = \sigma_0 pO_2^{\pm 1/n}$ are derived by combining the appropriate defect mass action relations with the electroneutrality condition and solving for $n = [e']$ and noting that $\sigma = nq\mu$ with μ the electron mobility for an *n*-type semiconductor [7, 8]. This has led to the development of resistive oxygen sensors based on TiO_2 [9 and references therein] or $SrTiO_3$ [10–12], which are operated at elevated temperatures to ensure fast defect equilibration in the bulk. Also for perovskite *p*-type materials at lower temperatures, a corresponding mechanism was used to explain sensitivity to reducing gases [13].

In the case of surface exchange sensors, the gas solid interaction is limited to the surface of the device. In the 1950s and 1960s, various research groups reported that metal oxides change their resistivity upon exposure to reducing gases at temperatures of ~400°C [14–16]. Shortly after this discovery, the first sensor devices based on tin oxide (SnO_2) were commercialized, with research extended to other metal oxide candidates. Numerous reviews on gas sensor devices of the so-called Taguchi type are available [10, 17, 18].

Soon after the discovery of the Taguchi type sensor, the corresponding mechanistic effects were investigated in more detail. The generally accepted model explains the underlying sensing mechanism for *n*-type semiconductors as described in the following [19].

On *n*-type semiconducting sensor surfaces, an oxygen adsorption layer develops in oxygen containing atmospheres [20]. The amount of adsorbed species is given by the fractional oxygen surface coverage θ, commonly defined as

$$\theta = \frac{\text{occupied adsorption sites}}{\text{total adsorption sites}} \quad (2)$$

Gaseous oxygen may adsorb as neutral molecular O_2 (physisorption) or atomic O (dissociative physisorption), generally at reduced temperatures. Due to their high electronegativity, the adsorbed oxygen molecules or atoms may also act as electron acceptors and form charged oxygen species by trapping electrons from the semiconductor, for example O_2^-, O^{2-}, or O^- (chemisorption). In the case of tin

[1] Assuming an *n*-type semiconductor

oxide sensors at $T>150°C$, dissociative chemisorption of oxygen was reported to be dominant [21, 22], although some controversy on this subject still persists [23]. Sophisticated models and experimental studies analyzing the nature and charge of adsorbed species on semiconductor surfaces have been proposed in the literature [24–26].

As shown diagrammatically in Fig. 2 in the case of oxygen adsorption on a *n*-type semiconductor, adsorbed charged species create additional surface states (with either acceptor or donor character) within the band gap of the semiconductor. Electrons trapped at these surface states induce a corresponding depletion of mobile charge carriers in the near-surface regions of the semiconductor. In terms of the band structure, adsorption of acceptor or donor like molecules leads to surface band bending, i.e., a surface potential Φ_s. This space-charge depletion layer, in turn, creates an electrically resistive surface region which can be readily detected experimentally.

The amount of charged adsorbates determines the height of the surface potential Φ_s, as well as the width d_s of the depletion layer (Fig. 2). Using Poisson's equation known from electrostatics, the following expressions can be derived as shown for example in [27, 28]

$$\Phi_S = \frac{\theta^2}{8e_0\varepsilon_0\varepsilon_r n_{bulk}} \tag{3}$$

$$d_S = \sqrt{\frac{2\varepsilon_0\varepsilon_r\Phi_S}{e_0 n_{bulk}}} = \frac{\theta}{e_0 n_{bulk}} \tag{4}$$

with e_0: electron unit charge, ε_0: permittivity of free space, ε_r: relative permittivity of the semiconductor, and n_{bulk}: bulk electron concentration.[2] Since the width d_s of the depletion layer depends strongly on the amount of charged adsorbates, any process that changes this amount, for example, a catalyzed oxidation reaction in the presence of a combustible gas, will directly affect the near-surface conductivity of the semiconductor. Various excellent reviews [29–31] summarize the effects in more detail, treating tin oxide as the model substance.

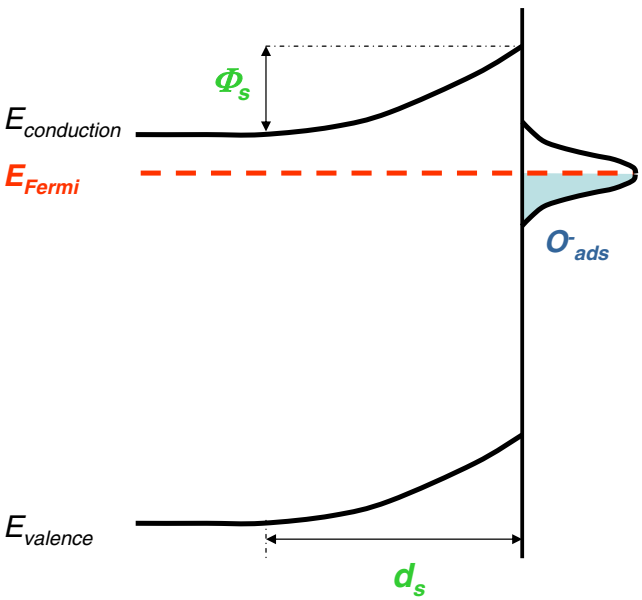

Fig. 2 Oxygen adsorption on *n*-type semiconductors: acceptor states, depletion layer, and band bending

Given that the mechanistic sensor effect is limited to the sensor surface, it is not surprising that sensor morphology and microstructure have been demonstrated to have an important impact on device performance [21, 30, 32–34]. While the quantitative influence of structural and textural parameters on sensor performance, e.g., grain size, interconnectivity of grains, surface-to-volume ratio, porosity and film thickness, is rather complex, it can be easily understood in a qualitative manner as illustrated in Fig. 3. Since the change in conductance of the sensing material is limited to the exterior regions of the grains, with the interior parts outside the depletion layer not contributing to the gas response, it then becomes clear that sensor performance must be, for example, substantially affected by grain size. That is, the conductance of smaller grains will be modulated more effectively than that of larger grains. This has been verified experimentally for various metal oxides (cf. Review [32] and references therein).

In the case of films with a given thickness, the presence of pores enables ready gas access to a large effective semiconductor surface. Mechanistic models therefore combine the gas–semiconductor interactions with diffusion equations depending essentially on microstructural parameters such as film thickness, porosity, and pore size [13, 35, 36].

In particular, the above findings sparked the trend to the nanoscale [18] and the need to precisely control film microstructure, porosity, and accessible surface area. For some years, research has focused on the preparation of the finest possible nanoparticles, quasi-1D-structures and nanostructured films to improve sensitivity. At the same time, various methods allowing for microstructure tailoring have also been proposed. As a consequence, novel deposition techniques aimed at producing well-defined nanostructures have been developed.

2.2 Potentiometric and amperometric devices

In addition to the use of semiconducting metal oxides for gas sensing, solid metal oxide electrolytes also represent an important category of attractive candidates for gas sensing. Resulting from the migration of ions through point defect sites in the lattice, these materials generally exhibit dominant ionic

[2] More precisely, n_{bulk} needs to be replaced by the effective bulk concentration of ionized donors $[D^{\bullet}]_{eff}$.

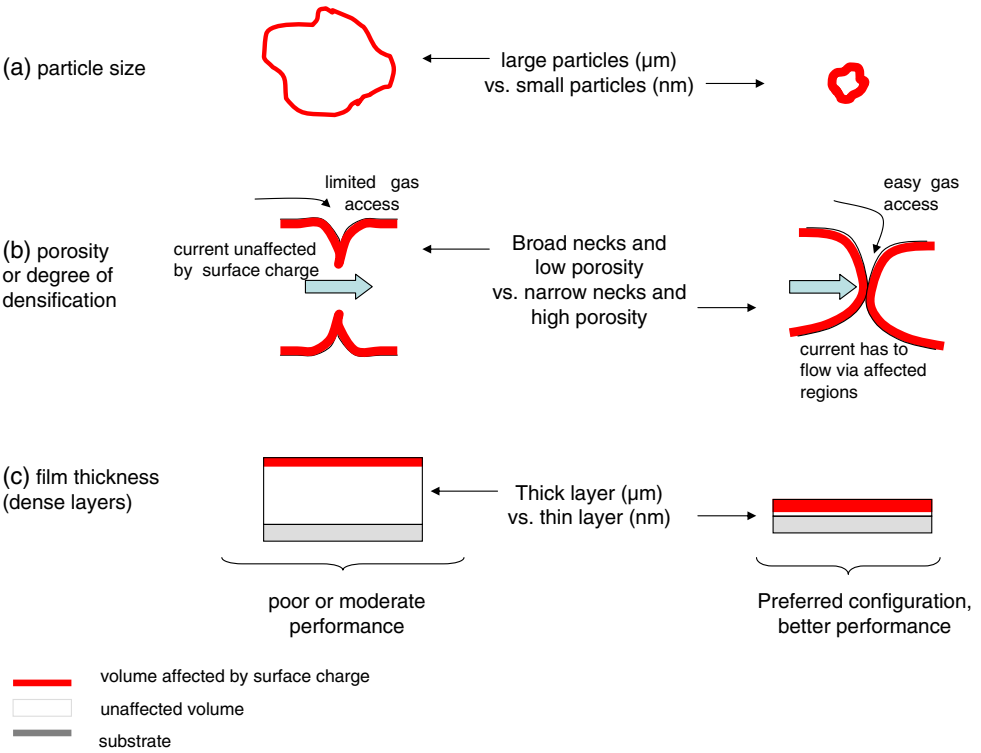

Fig. 3 Impact of various microstructure parameters on gas sensing performance in the case of the Taguchi type conductometric sensor

conductivity with conductivity values $\sigma \geq 10^{-5}$ S/cm and ionic transference numbers $t_{\text{ionic}} = \sigma_{\text{ionic}}/\sigma_{\text{total}} > 0.99$. Electrochemical cells based on such solid electrolytes may be employed for sensing chemical species in a very selective and accurate manner [37].Among these candidates is the zirconia-based air-to-fuel (or lambda) sensor for automotive applications and oxygen sensor used in steelmaking. The high oxygen ion conductivity in zirconia (a 0.9 ZrO_2–0.1 Y_2O_3 solid solution) is due to the large number of oxygen vacancies created in the solid in order to charge compensate for the lower valent Y^{3+} ion substituting on the Zr^{4+} lattice sites.

Three main types of electrochemical solid state sensors are distinguished, i.e., potentiometric, amperometric, and mixed potential devices. These concepts are discussed briefly in the following. More detailed reviews on *ceramic* electrochemical sensors, discussing the respective mechanisms, are available for example in [37, 38].

In the exemplary case of oxygen sensing, the potentiometric measurement based on an electrochemical concentration cell with a solid metal oxide electrolyte. By preparing a gastight oxygen ion conducting membrane or sintered body, the atmosphere to be measured is separated from a reference gas with fixed pO_2, usually an internal air channel ($pO_{2,\text{reference}}$= 0.21 bar). At the noble metal electrodes applied on either side of the electrolyte, equilibrium of the redox reaction

$$^1/_2 O_2 + 2e' \Leftrightarrow O^{2-} \tag{5}$$

is established. According to the Nernst equation (Eq. 6), a thermodynamically well defined potential drop or electromotive force develops across the cell, expressed as a function of T, $pO_{2,\text{measure}}$ and $pO_{2,\text{reference}}$ by.

$$\text{emf} = \frac{RT}{4F} \ln\left(\frac{pO_{2,\text{measure}}}{pO_{2,\text{reference}}}\right) \tag{6}$$

In which R is the gas constant and F the Faraday constant. By measuring emf and T with $pO_{2,\text{reference}}$ known, $pO_{2,\text{measure}}$ can thus be calculated.

As a variation of the solid state potentiometric sensor, amperometric oxygen sensor devices with a current readout have been developed [1, 37]. In this approach, which requires no reference channel, a diffusion barrier is added on top of the oxygen insertion electrode. A fixed voltage is applied to the electrolyte to pump oxygen ions through the electrolyte thereby drawing oxygen through the diffusion barrier. At low voltages and high enough pO_2, where there is sufficient diffusion of oxygen through the barrier to provide enough oxygen at the surface of the solid electrolyte to satisfy the oxygen ion flux through the electrolyte, the pumping current is a linear function of the applied voltage according to Ohm's law. At higher voltage, however, the system becomes diffusion limited, and any oxygen molecules arriving at the electrolyte surface are pumped away immediately. The corresponding limiting current is voltage independent and a function of the oxygen partial pressure. Care must be taken in the choice of applied voltage, which must be large enough to establish limiting current conditions but should not exceed the electrochemical potential required for the electroreduction

of the electrolyte or, in the case of humid conditions, water electrolysis.

In the electrochemical cells discussed till now, the mobile ionic species in the electrolyte corresponds to the gaseous species to be detected. However, such electrolytes are not available for every analyte gas of interest. Therefore, another potentiometric sensor configuration has been investigated involving the use of an additional porous auxiliary phase coated onto the measuring electrode. At the reference electrode, the activity of the mobile ion is fixed. Suitable materials for auxiliary phase fulfil two requirements, (a) they interact with the analyte gas and (b) they contain the same ion species as the electrolyte. For example, porous $NaNO_3$ or $AgNO_3$ films are used for NO_x detection in combination with a sodium or silver ion conductor such as Nasicon (Na-super ionic conductor, $Na_{1+x}Zr_2P_{3-x}Si_xO_{12}$ with $0 \leq x \leq 3$) or Ag-β''-Al_2O_3. Similar concepts have been developed for CO_2 or Cl_2 detection [39–41].

Mixed potential sensors form another subgroup of potentiometric gas sensing devices. This type of sensor features a solid electrolyte equipped with two electrodes exhibiting different catalytic activities, e.g., Au and Pt. In this case, the voltage read-out is generated from two or more competing reactions occurring at each of the electrodes. Since the catalytic performance of each of the electrodes is different, a different mixed potential is established at each electrode, and a voltage drop across the device is detected.

In either case outlined above, the sensor is prepared from multilayer structures combining different materials, microstructures and functionalities. In general, the electrolyte needs to be dense to provide good ionic conductivity and/or to separate the reference and measuring sides of the device. As to the electrodes and the auxiliary phase, on the other hand, high porosity is required. Hence, the choice of optimum deposition techniques is crucial for the development of high-performance electrochemical devices.

2.3 Field effect transistors

Capacitors, Schottky diodes, and field effect transistors are widely used electronic devices. Chemical sensors based on these devices have been under development for some years. To enable high temperature applications, silicon carbide-based diodes or FETs have been investigated. Silicon carbide FETs function as chemical sensors when a catalytic metal, e.g. Pt, Ir or Pd, is used as the gate electrode. Several groups have contributed to the development of the SiC field-effect or capacitive sensor devices [42–46].

Analyte molecules such as hydrogen or hydrocarbons are detected following adsorption in pores close to the gate–channel interface or following dissociation on the surface of the catalytic metal with the resulting hydrogen atoms diffusing through the gate material to the insulator surface. This creates a polarized layer on the surface of the insulating layer [47], which in turn induces a change in the number of mobile charge carriers in the channel resulting in a change in e.g. the threshold voltage of a FET or the flat band voltage of a capacitor.

For both the Schottky diode and the MOSFET gas sensor device, it is desirable that the deposition techniques used be compatible with standard FET processing and ideally provide direct-write features for patterning the gate directly rather than using complex photolithographic methods.

2.4 Surface and bulk acoustic waves (SAW and BAW)

The presence of analyte gases is detected via changes in resonant frequency, acoustic wave velocity or loss in surface and bulk acoustic wave devices. A common bulk acoustic wave (BAW) device is the piezoelectric quartz crystal micro-balance (QCM), which is commonly used for the detection of mass changes via a shift in the resonant frequency of the piezoelectric material. For sensor purposes, the QCM transducer is coated with a gas sensitive layer. Any mass change Δm of the coating, induced by adsorption or reaction with the target analyte, is directly translated into a measurable shift in resonant frequency Δf according to the Sauerbrey equation [48]

$$\Delta f = -\frac{f_q^2 \Delta m}{N \rho_q S} \tag{7}$$

where f_q is the fundamental resonant frequency of the device, N the frequency constant of the specific crystal cut ($N_{AT} = 1.67 \times 10^5\ Hz\,cm$), ρ_q=2.65 g/cm^3 the quartz density and S is the surface area covered by the mass-sensitive film.

Surface acoustic wave (SAW) devices have shown promising characteristics as chemical gas sensors due to their small size, low cost, fast response and high sensitivity. As in BAW devices, a coating interacting with the analyte gas is deposited on the device surface. The analyte is reversibly adsorbed on the coating resulting in a mass increase. This mass change modifies the SAW velocity in the device, which is measured indirectly using the device as a resonant element in a delay line (DL) oscillator circuit and measuring the frequency shift due to the gas adsorption.

In either the SAW or the BAW devices, organic materials are commonly used as gas sensitive coatings. Some metal oxides have been applied as well. Next generation deposition techniques for this transducer type should yield thin films with well-defined porosity and ideally provide direct-patterning options to precisely position the functional layer.

In conclusion, future deposition techniques for the various types of metal oxide sensors discussed above should meet the following requirements.

- Allow precise control of film microstructural features.
- Readily integrate with microelectronic and/or micromachined structures.
- Offer direct write capability to ensure precise positioning of functional films.
- Provide inexpensive and easy to handle process steps.

3 Traditional deposition techniques

This section describes deposition techniques commonly used in sensor device fabrication, e.g. screen-printing, physical and chemical vapour deposition (PVD and CVD) and sol–gel based methods. Review [49] assesses the use of these techniques for micromachined conductometric sensors. A simplified, but instructive link between these deposition techniques and the microstructural features (cf. Section 2.1) is provided. While both CVD and PVD methods mostly result in compact layers comparable to Fig. 3(c), porous films (Fig. 3(a) and (b)) are generally obtained by traditional thick-film techniques, e.g. screen-printing.

Although well-established, these methods present two crucial limitations. First, the microstructure control achievable via these processes is limited and in most cases insufficient. In addition, their direct-write ability is extremely poor. In general, time-consuming post-processing techniques, for example photolithographic structuring, are required. The use of masks or screens with a fixed pattern also limits versatility of these traditional processes.

3.1 Screen-printing

Screen-printing is a low-cost, simple and highly popular manufacturing technique, appropriate for mass production. A thixotropic paste prepared from the precursor material and organic vehicles is applied on top of the screen, a finely woven mesh of either stainless steel wires or polymer fibers mounted under tension on a metal frame. The backside is covered with a photosensitive emulsion upon which the desired screen pattern is formed by photolithography. A squeegee traverses the screen under pressure and forces the paste to flow through the mesh. The pattern is thus transferred onto the substrate.

Typical film thicknesses achievable by this 2D technique range from 5 to 50 μm. The lateral resolution, which is a function of mesh size and ceramic paste properties, is limited to about 75 μm.

3.2 Sputtering

Sputtering is a convenient technique for depositing metallic and inorganic thin films. The sputtering process consists of a target, i.e., a plate of a stoichiometric mixture of the material of interest, and a substrate placed on a grounded sample holder positioned at some distance from the target. By applying power to the target in a controlled gas atmosphere, a glow discharge, i.e., a partially ionized gas of ions, electrons, and neutral species, is initiated in the target vicinity. Due to collisions between the ionized gas and target, material is ejected and travels to and nucleates onto the substrate. The thin film thickness is a function of the duration of this process with typical values ranging from 0.1 to 0.8 μm [50]. The sputtering gas can be chosen inert or reactive (e.g., Ar-oxygen mixtures) to promote additional chemical reactions during deposition.

The use of a radio frequency (RF) generator is essential to maintain the discharge and to avoid charge build-up when sputtering insulating metal oxides. In addition, magnets are used in magnetron sputtering to enhance the sputtering rate. The magnetic field traps electrons in the vicinity of the target and thus increases the ionization. Since the trapping effect at the target does not only affect electrons, but also charged gas ions, this prevents impurities from reaching the substrate, and film quality may be improved.

One limitation of the sputtering process is the so-called shadow effect due to the line of sight nature of the trajectories followed by the emitted target particles. Parts of the substrate that are, for example, hidden by gratings or undercuts cannot be covered.

3.3 Thermal evaporation and pulsed laser deposition

Thermal evaporation is a high vacuum technique ($p < 10^{-4}$ mbar) suitable for the deposition of optical films as well as thin films needed in integrated circuits and electronic devices. Thermal energy is provided to the target material either by irradiation or by resistive or inductive heating. The target material evaporates, diffuses, and eventually crystallizes on the substrate placed close to the target. The main limitation of the evaporation process is that the vapor composition depends largely on the individual vapor pressures of the elements in the target material. Hence, the deposition of multi-component materials, with well-defined stoichiometry, becomes very difficult.

Pulsed-laser deposition (PLD) was first used to deposit high-temperature superconducting thin films based on $YBa_2Cu_3O_{7-\delta}$, a metal oxide of complex stoichiometry. Since then, many materials that are normally difficult to deposit by other methods, in particular multi-element oxides, have been successfully deposited by PLD. This

feature derives from the laser material removal mechanism, which relies on a photon interaction with the target. A vapour plume of material is created and collected on a substrate placed a short distance from the target. Though the actual physical processes of material removal are quite complex, one can consider the ejection of material to occur due to a rapid explosion of the target surface due to superheating. Unlike thermal evaporation discussed above, the laser-induced expulsion produces a plume of material with stoichiometry similar to the target. As a consequence, it is generally easier to obtain the desired film stoichiometry for multi-component materials using PLD than with other deposition technologies. Depending on the optics used, features can be achieved with a resolution between 30 and 200 μm.

3.4 Chemical vapour deposition (CVD)

Chemical vapour deposition, a process used to produce high-purity, high-performance solid thin films, is widely used in the semiconductor industry as part of the semiconductor device fabrication process. A number of forms of CVD are in wide use, which essentially differ in process conditions and in the means by which chemical reactions are initiated (e.g., activation process). In a typical CVD process, the substrate is exposed to a gas stream containing one or more volatile precursors. These react and/or decompose on the substrate surface to produce the desired film material. In contrast to physical vapour deposition, there is no shadow effect, and even complex shapes are coated uniformly. Film thicknesses range from one monolayer to 100 μm, and by optimizing the deposition conditions, nanocrystalline films can be prepared. While the CVD process offers significant advantages for film deposition including spatial control and excellent reproducibility, it presents limitations with respect to porous and multi-dimensional structures, since there is little flexibility for tailoring the structure beyond control of the nanoparticle size [51].

3.5 Sol–gel based: dip and spin coating

The spin-coating technique utilized in various industrial applications such as photo-resist coating, in microfabrication, or in the fabrication of nanoparticle assemblies, is one of the most established wet coating methods. As the precursor, the target material is mixed with a volatile solvent, which evaporates during the spinning process. After placing this precursor on the substrate, the substrate is then rotated at high speed in order to spread the fluid by centrifugal force. Film thickness depends on the applied angular spinning speed as well as on the concentration of the solution and the solvent. Thin films with thicknesses below 10 nm can be achieved.

In dip coating, a substrate is immersed in a coating bath usually consisting of a polymeric or particulate sol. Upon withdrawal from the bath, the substrate retains a boundary layer. At the same time, the solvent begins to evaporate. The rate of evaporation, which depends on withdrawal velocity and drying conditions, is reported to have an impact on the microstructure of dip-coated particle-assembly structures. When the drying front recedes into the pores of the particulate network, capillary pressures—depending on pore size—may occur, thus compacting the structure. This drying step, i.e., the evaporation of the solvent, is a major challenge in both wet-phase coating techniques. During this stage, cracks are difficult to avoid, and film quality depends strongly on the precise control of drying conditions.

4 Novel methods: beyond CVD, PVD, and screen-printing

Numerous novel deposition techniques have been developed to improve the performance of functional layers and to facilitate their integration into real-world, mass-market applications. In the case of conductometric sensors, it is of great interest to precisely control the micro- or even nanostructure of the metal oxide films in order to improve sensor performance. In Reference [50], for example, the above-mentioned classical techniques as well as several novel methods are evaluated for the preparation of nanocrystalline, semiconducting films and their integration with microelectronic platforms. At the same time, direct-write features are required for integration of metal oxide films onto sensor platforms based on micromachined FET or SAW devices. In addition, direct write techniques have the potential to simplify the fabrication of miniaturized sensor arrays.

This section focuses on novel deposition methods that have been reported in the literature for metal oxide gas sensor fabrication. They are grouped in the following six subsections:

- soft lithography: microcontact printing, micromolding in capillaries (MIMIC)
- direct writing: matrix assisted pulsed laser evaporation (MAPLE), ink-jet, 3D-printing/micropen
- Films: flame spray pyrolysis, thermal spray direct writing
- Structure replication: templating and use of rigid matrices
- nanofibers: vapor–liquid–solid (VLS), vapor solid (VS), nano-carving
- electric-field assisted: electrospinning/-spraying

The first two groups aim at facilitating patterning and/or direct writing. The methods in the third group provide simple, inexpensive tools for preparation of well-controlled

multilayered structures. Finally, the last three subgroups emphasize the trend for precise tailoring of the micro- and even nano-features of gas sensitive devices.

4.1 Soft lithography

The term "soft lithography", a low cost alternative to traditional photolithography, describes a patterning technology that allows the shaping of colloidal suspensions on a μm scale. The core element of the process is an elastomeric mold of the desired micropattern which is prepared by polymerizing an appropriate organic precursor around a positive master mold [52]. In most cases, poly dimethylsiloxane (PDMS) is the polymer of choice. The present subsection focuses on two examples of this technique, micro contact printing and micromolding in capillaries (MIMIC), both of which have been used for the preparation of gas sensor devices [53]. A schematic of both processes is depicted in Fig. 4.

In micro contact printing, the patterned PDMS mold is used as a stamp to transfer an appropriate organic solution onto the substrate to be patterned (cf. Fig. 4(a)). Hydrophobic and hydrophilic regions are created on the substrate, which is then dipped into a colloidal suspension of the coating material. During the dip coating process, the suspension wets the substrate selectively, and the desired micropattern is replicated with a resolution of 5 μm [53, 54], well below the typical resolution limit of screen-printed patterns. Heule et al. successfully prepared tin oxide patterns with this technique, using powder suspensions with 1/3 solid content (primary particle size d_{50}: 220 nm). A final line width of 20 μm was obtained [54]. Lim et al. [55] investigated ZnO thin films prepared by microcontact printing for gas sensor applications. The devices were exposed to CO, NO, and propane at elevated temperatures in the range from 200°C to 400°C and showed a sharp resistance change.

In the case of the MIMIC process presented in Fig. 4(b), the PDMS mold is placed on top of the substrate. Due to the particular elastomeric properties of PDMS, a very tight but reversible contact is established. The suspension to be deposited is then drawn into the channels of the stamp due to capillary forces [56] or by the application of a vacuum [57]. Heule and Gauckler used the MIMIC process to create microlines of gas sensitive SnO_2 [56] or In_2O_3 [53], with typical width of 3 μm. In this manner, arrays of nanostructured sensor elements, each covering an area of 10× 30 μm, on a single microhotplate were successfully prepared (cf. Fig. 5). Initial device performance tests towards CO

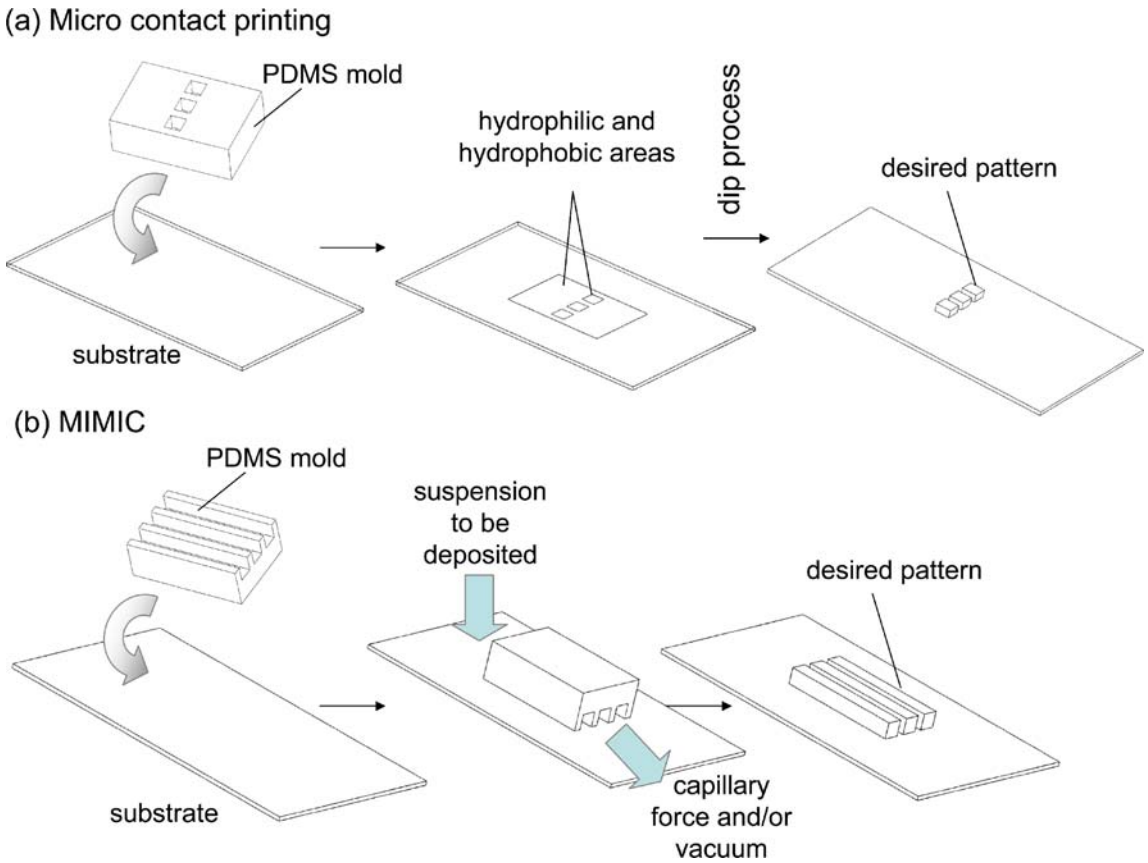

Fig. 4 Soft lithography—scheme of micro contact printing (**a**) and micromolding in capillaries (**b**)

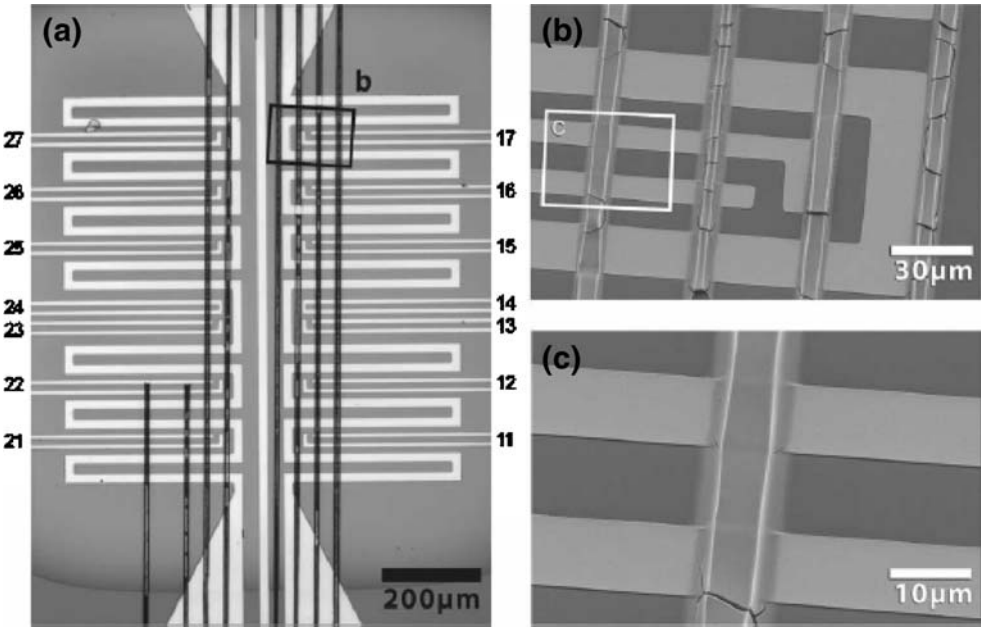

Fig. 5 Tin oxide microlines by MIMIC on sensor platform. Reprinted from [56], with permission from Elsevier

pulses yielded promising results. The detection limit of undoped tin oxide lines was estimated to be 600 ppm while in the case of In_2O_3, 30 ppb of ozone could be detected.

4.2 Direct writing: ink-jet, 3D-printing/micropen, MAPLE

In recent years, the potential of direct-write technologies, which allows the direct patterning of structures without use of masks, has been investigated. These techniques include plasma spray, laser particle guidance, matrix-assisted pulsed-laser evaporation (MAPLE), micropen, ink jet, e-beam, focused ion beam, and several novel liquid or droplet micro-dispensing approaches [58]. Since both materials and processing requirements are being met with increasing success, these techniques are now finding themselves in a growing range of applications including printed circuit boards, passive electronic components, tissue engineering, and biosensor arrays [58]. In the field of chemical gas sensing, few references have been reported in the literature to date.

In general, direct-write techniques require trade-offs between increased particle bonding, resolution, or speed. Nowadays, speeds greater than 200 mm/s and line resolutions on the micrometer scale are feasible while maintaining material properties comparable to those of conventional screen-printed materials [58]. Thus, lower prototyping and production costs and time, increased manufacturing flexibility, and higher manufacturing yields are envisioned.

4.2.1 MAPLE (matrix assisted pulsed laser evaporation)

MAPLE is a technique based on pulsed laser deposition, which provides a gentle mechanism to transfer small and large molecular weight species from the condensed phase into the vapor phase. It is of particular interest for polymer and biomaterial thin film deposition, but it has also been applied to metal oxides and nanocomposite materials [58–60]. The smallest feature resolution that may be achieved with this 2D method is in the range of 10 µm. The material to be deposited is diluted in a volatile organic binder or matrix with a concentration of a few percent by weight. For MAPLE direct write, the resulting composite is applied as a uniform coating on a transparent carrier placed at some distance from the substrate as shown in Fig. 6. The film is then irradiated from the backside with a laser beam following the desired pattern. The laser energy is principally dissipated by the matrix and converted into thermal energy, thus vaporizing the organic binder. With the evaporating matrix, also molecules of the material of interest are transferred to the gas phase and are transported to the substrate placed some distance from the target. There, the target material is deposited. While in some cases, the sticking coefficient of the binder vapor can be considered nil, other applications require high-temperature annealing steps to remove the remaining binder.

In terms of sensor applications, this technique was initially employed with focus on thin organic layers of metal acetylacetonates for solid-state gas sensors [61]. Rella et al. [59] then transferred this approach for the purpose of uniformly depositing titania nanoparticles onto alumina substrates. A uniform coverage of the substrates was obtained. When exposed to ethanol and acetone in ppm concentrations, the devices yielded promising results at operating temperatures from 350°C to 400°C.

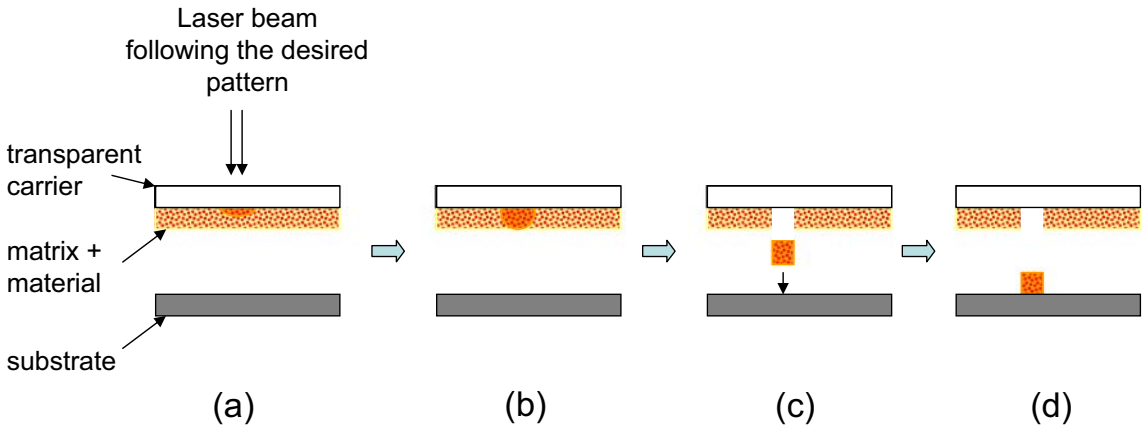

Fig. 6 Scheme of MAPLE-direct write. The laser path writes the desired pattern. For each pixel, the laser irradiates the matrix/material film deposited on the transparent carrier substrate (**a**). The laser energy is dissipated, and a fraction of the matrix evaporates (**b**). The vapor, which also contains the material of interest, is transferred to the substrate (**c**), where it eventually forms one pixel of the pattern (**d**)

4.2.2 Ink jet

Due to its unique advantages, including direct patterning, low cost, potential for high throughput combinatorial chemistry, and low materials waste, ink-jet printing has received much attention in materials science and device preparation [62, 63]. Besides organic films for organic LEDs [64] or metal electrodes for thin film transistors [65], particle suspensions [66] and complex oxide compounds [67–70] have been successfully deposited. In terms of sensors, inkjet printing is ideal for directly preparing thin-film sensor arrays that require multiple depositions, lithography, and etch processes.

Similar to devices used for home desktop publishing, the printer propels well-dispersed colloids of ceramic powder in the form of drops of ink from the print-head to create multiple layers of images, each controlled by digital data from a computer. For ceramic processing, low viscosity inks (4–20 mPa s) consisting of solvent, powder, binder, and dispersants are typically used [66]. In these cases, feature sizes in the range of 70 μm are achievable.

Shen et al. [71] prepared ZnO based gas-sensing thin films by ink-jet printing using a commercial printer. Sol–gel ZnO inks with appropriate viscosity and surface tension were prepared as precursors. The range of achievable film thicknesses and the possibility of integrating dopants were investigated. Film functionality as acetone sensors was studied with R_0/R response towards 180 ppm acetone yielding maximum values of 8–9 depending on doping and operating temperature. Lee et al. [72] used inkjet-printing to prepare tin oxide channel layers for a metal insulator semiconductor field-effect transistor (MISFET). They reported the films to be porous with a graded pore structure after annealing in air at 500°C (cf. Fig. 7).

The versatility of ink-jet printing is also of interest for multi-component inks. One example is the use of polymer microbead templates that have been used to enhance the surface area of functional ceramic films [51, 73, 74]. Conventionally, a suspension containing the ceramic precursor plus polymer (poly-styrene or poly-methylmetacrylate) beads with well-defined, homogeneous diameter is prepared. During heat treatment following deposition, the polymer decomposes, resulting in a highly porous ceramic scaffold with exceptionally large surface area. For example, this method was investigated in [73] for the preparation of QCM-based mass sensitive NO_x sensors with $BaCO_3$ as the gas sensitive coating. The films were deposited by simple drop casting, resulting in ill-defined film thicknesses and poor adhesion. Sahner et al. then transferred the templating method to ink jet printing using heterogeneous inks containing both polymer templates and $BaCO_3$ precursors (Sahner et al., in preparation). The inks were prepared using barium acetate and poly-methylmethacrylate microspheres with 800 nm diameter as precursors. Commercial 5 MHz AT-cut quartz crystal microbalances equipped with Au electrodes served as the resonant platform. A semi-automated thermal ink-jet printer was used in this study. For layer deposition, the substrates were positioned on a computer-controlled automated *x*–*y*-stage under the static printhead, and patterns were deposited pixelwise. Figure 8 presents a sample of the complex patterns achieved with this set-up.

4.2.3 3D-printing

Besides widespread technological applications in tissue engineering, advanced functional ceramics and composites, three-dimensional periodic structures prepared from colloids may be useful for gas sensor devices [75]. Robo-casting, automated direct-ink writing, three-dimensional printing (3DP), or micro-pen writing offer a powerful route for producing complex periodic 3-D structures at length scales from micrometers to millimetres [76–78]. According to the

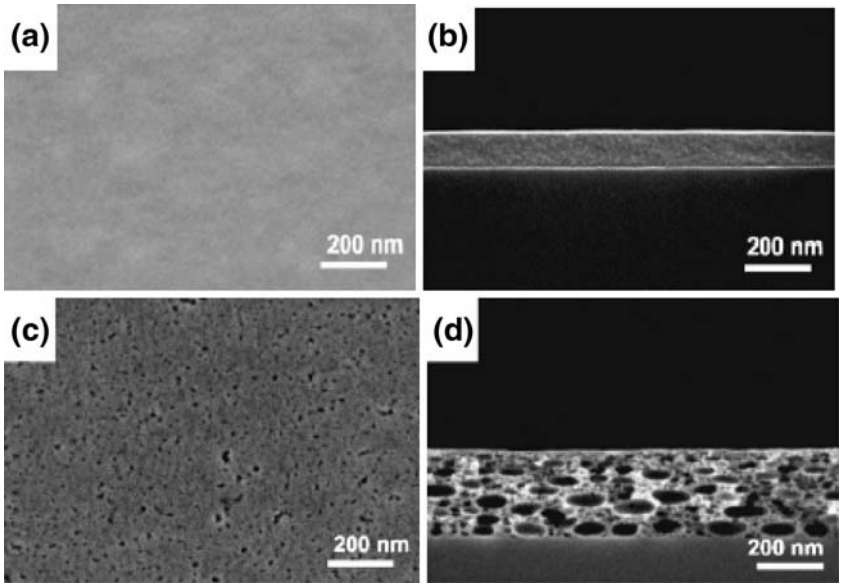

Fig. 7 SEM micrographs of ink-jet printed SnO_2 films. *Top row*: as deposited film, top view (**a**) and cross section (**b**). *Bottom row*: after thermal treatment at 500°C in air, top view (**c**) and cross section (d), showing the graded pore structure [72]. Reproduced by permission of ECS—The Electrochemical Society

scheme depicted in Fig. 9, a computer-controlled writing nozzle moves over the substrate. As precursors, highly concentrated colloidal suspensions are used that solidify either by liquid evaporation or a temperature-induced phase change. The preparation of well-defined periodic structures including unsupported elements spanning gaps places high demands on suspension design, which must satisfy a number of criteria. First, it must exhibit a well controlled viscoelastic response to flow through the nozzle. Second, upon contacting the substrate, it must solidify nearly immediately. Third, a high colloid volume fraction is required to minimize shrinkage [75, 80]. With this technique, minimum line widths tend to be in the range of 200 μm.

Smay, Lewis, and coworkers studied three-dimensional printing (3DP) techniques to prepare well-defined $BaTiO_3$ ceramics [79], $Pb(Zr,Ti)O_3$ piezoelectrics [81] and photonic crystals [82] (cf. sample patterns shown in Fig. 9). As to gas sensor applications of 3D-printed structures, initial studies were conducted which utilized titania grids prepared by 3DP [83] for NO_x sensing (Rothschild, in preparation).

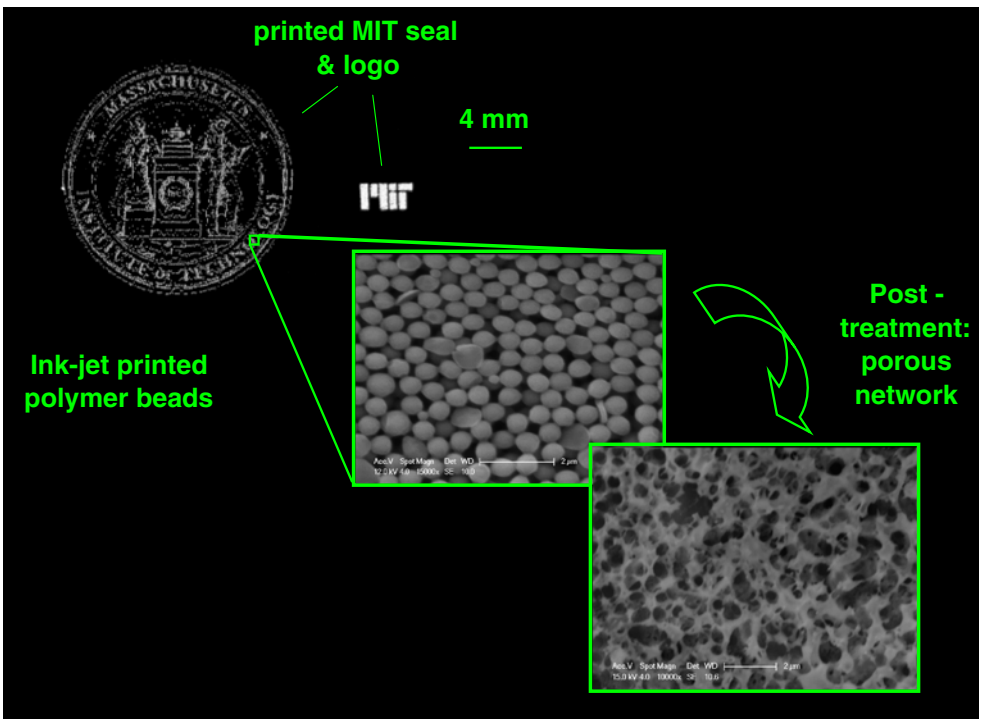

Fig. 8 Example of ink-jet printed patterns using the microsphere templating technique gas sensitive material

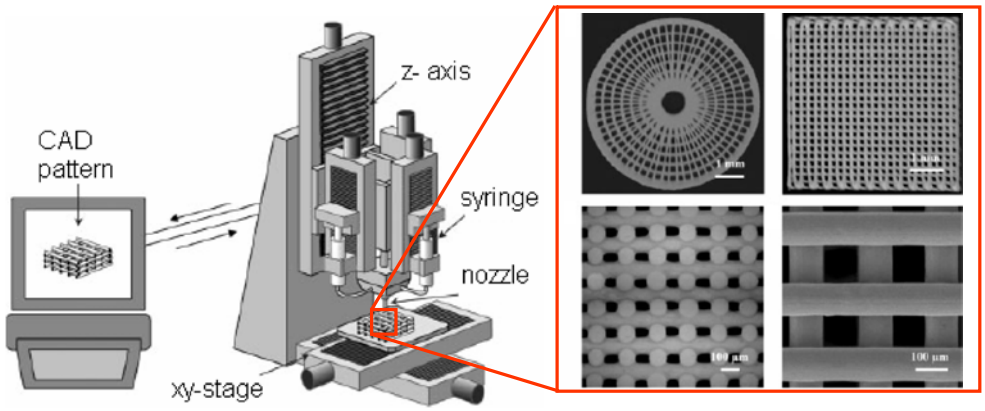

Fig. 9 *Left*: Principle of the direct assembly of nanoparticle inks via 3DP. A syringe containing the ink is mounted on a *z*-axis motion stage with the ink deposited through a nozzle onto a substrate placed onto a moving *x*–*y* stage. Stage movement is controlled using a CAD file of the desired 3-dimensional pattern. Right: Examples of 3DP structures assembled from $BaTiO_3$ nanoparticle inks [79]. Copyright Wiley-VCH Verlag GmbH & Co. KGaA. Reproduced with permission

4.3 Film deposition by in-situ flame spray pyrolysis and direct write thermal spray

Suspension-free spray deposition techniques from the gas phase present a mayor advantage over the wet sol-gel based coating methods, since no solvent need evaporate. Hence, the films are less prone to cracking, and are more homogeneous, reproducible and comparable to films produced by CVD or PVD [84]. Depending on the deposition conditions (gas flow rate, distance between substrate and source) and substrate temperature, dense layers, preferable for protective coatings or porous films for sensing and catalysis applications, may be obtained.

Flame spray pyrolysis (sometimes denoted as combustion CVD [84, 85]) is a versatile and effective technique to produce metal oxide powders and to deposit thin films for various industrial applications, for example the commercial fabrication of optical fibers for telecommunications and deposition of doped-silica particles having closely controlled refractive indices for light transmission [84]. Many different materials, including various metal oxides, have already been deposited using this technique, which offers the possibility to control film morphology and powder particle size in the nm range [84]. After formation in the flame by nucleation, coagulation, and coalescence, nanoparticles undergo direct (in situ) deposition onto suitable sensor substrates. A very fast and clean single step process for sensor preparation is thereby obtained. The resulting thick films are highly porous and present a large accessible surface, which makes flame spray pyrolysis a promising candidate for rapid and low cost sensor production. The quality and properties of the films and powders depend on the process parameters.

In [86], Mädler et al. prepared highly porous pure or Pt-doped SnO_2 powders by direct flame spray synthesis. Subsequently, the powders were screen-printed and annealed at temperatures up to 500°C. A detection limit for CO well below 10 ppm was observed. Using a similar set-up, Liu et al. conducted deposition at higher temperatures (up to 850°C) [85]. These as-deposited films were directly functional as gas sensor layers exhibiting very good ethanol sensing behaviour. Sahm et al. investigated this approach to synthesize SnO_2 and Al_2O_3 nanoparticles, with and without Pd doping, directly deposited from the aerosol phase by thermophoresis onto standard sensor substrates forming highly porous films [87]. Metal organic precursor solutions were used [88, 89]. By repeating layer deposition, multilayer sensors as shown in Fig. 10 were prepared consisting of doped and undoped gas sensitive SnO_2 and Al_2O_3 as a filter layer.

The operation principle of thermal spray direct write is similar to flame spray pyrolysis discussed above. During thermal spraying, the material to be deposited is melted by a high temperature torch. The molten particles are accelerated and reach the substrate, where they rapidly solidify forming thick films [90]. Since the substrate itself is not heated, the technique enables deposition of most materials onto low temperature substrates, such as plastics [91]. The main applications of this directed melt spray process have been protective coatings against wear, heat, corrosion, and oxidation. Since the potential advantages of thermal spray include high speed direct writing capability, cost effectiveness, and useful materials properties in the as-deposited state, it has recently been developed as a direct writing technique for electronic devices. Ahn et al. prepared impedancemetric ceramic humidity sensors consisting of a spinel ($MgAl_2O_4$) dielectric layer equipped with Ni-Al electrodes by direct-write plasma spraying [92].

4.4 Structure replication

To create ordered mesoporous metal oxide networks, two different approaches, nanocasting and the utilization of amphiphilic templates, have been reported in the literature [93].

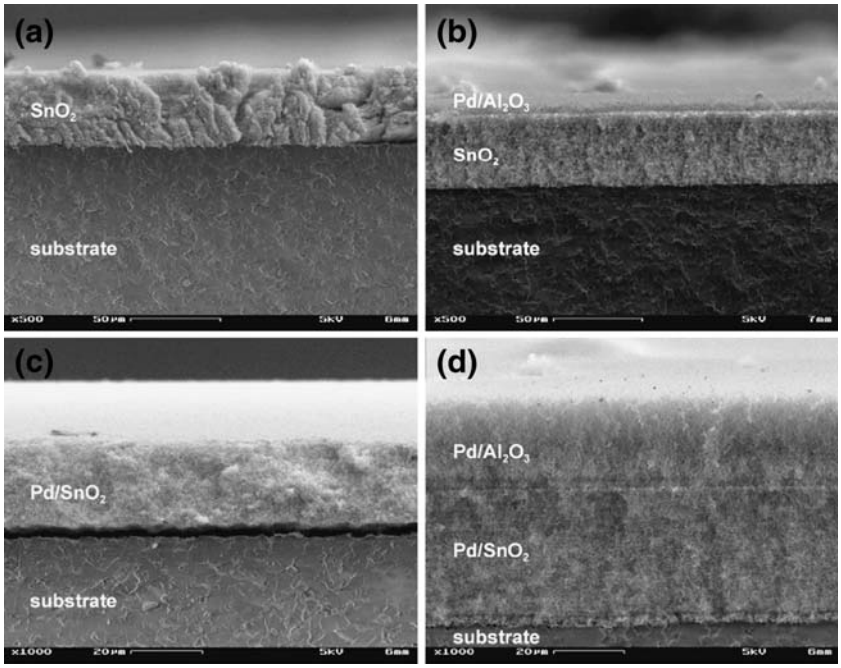

Fig. 10 SEM cross section of various multilayer structures prepared by in-situ flame spray pyrolysis. Reprinted from [87], with permission from Elsevier

Templating has become a standard procedure to synthesize mesoporous inorganic structures, mainly based on silica building blocks or zeolites (aluminosilicates). In general, the structure-directing templates are amphiphilic species such as block co-polymers or surfactants. As shown in Fig. 11, these are dispersed in a solution of the inorganic precursor, where they self-assemble spontaneously as micells. During synthesis, a solid network crystallizes around the self-assembled units and replicates the periodic structure following which the organic templates are removed.

Although the process has been used primarily for silicates and related structures, mesoporous products of two important gas sensor materials, SnO_2 and WO_3, have also been prepared by the templating technique. Li and Kawi [94] synthesized stable mesoporous SnO_2 materials, using sodium stannate as the starting precursor and cationic surfactant as the synthetic template. In their study, they systematically evaluated the effect of sensor surface area on sensor sensitivity and reported a linear dependency. The Egashira group prepared large mesoporous SnO_2 powders by employing $SnCl_2$ H_2O as the tin source and the self-assembly of a triblock copolymer as a surfactant. The powders exhibited very large surface areas up to 253 m^2/g and a stong response towards hydrogen [95].

Nanocasting relies on the use of a mesoporous, rigid silica matrix as a "mold". The molds are prepared by the templating method described above and then filled with a precursor solution of the target metal oxide. As an

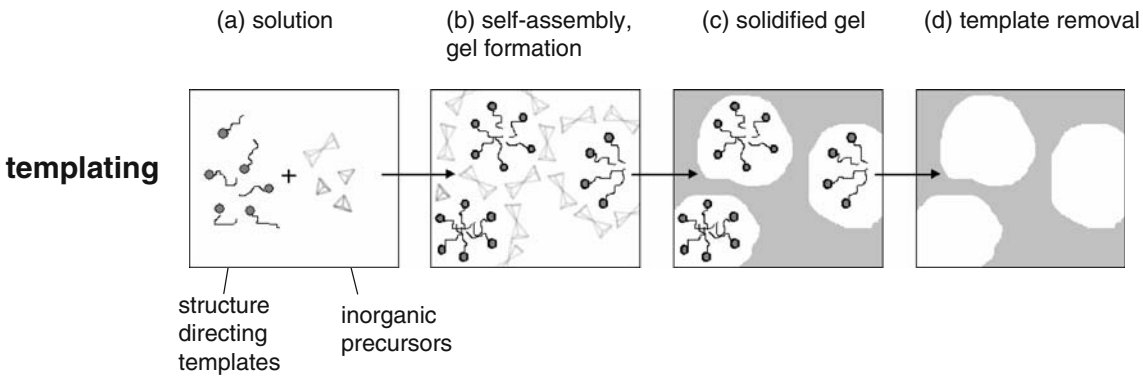

Fig. 11 Scheme of the templating method. First, a solution containing both organic amphiphilic templates and inorganic precursors is prepared (**a**). The organic species spontaneously self-assemble into periodically arranged micelles (**b**). These are surrounded by the remaining solution containing an increasing concentration of the inorganic species. Eventually, the crystallization limit of the inorganic precursor is reached, and a solid network is formed (**c**). In a final step (**d**), the organic template is removed [93]. Copyright Wiley-VCH Verlag GmbH & Co. KGaA. Reproduced with permission

advantage over conventional sol–gel templating routes, which in general require aqueous reaction media and are hence limited to T<200°C, the rigid matrix withstands the high temperatures that are needed for formation of the target oxide. Thus, higher degrees of crystallinity are obtained without loss in the periodic structure. After the thermal conversion step, the matrix is etched away either with hydrofluoric acid or concentrated sodium hydroxide. Hence, the metal oxide forms the negative replica of the initial porous network as depicted in Fig. 12.

The Morante group investigated multiple mesoporous metal oxides obtained by the nanocasting technique [96–98]. In the case of WO_3 based NO_2 sensors [97, 98], they compared two different crystalline mesoporous replicas (2D hexagonal structure vs. 3D cubic structure) obtained by using different silica materials as templates. Compared to the 2D replicas, the 3D structures presented a stronger response to NO_2 as well as a shorter response time. This was attributed to the higher surface area of the 3D replica, as verified by Brunauer–Emmett–Teller (BET) analysis.

While useful for a great variety of gas sensitive metal oxides such as Fe_2O_3, WO_3, Cr_2O_3 and In_2O_3 [93 and references therein], this method is not suitable for amphoteric oxides such as ZnO due to the chemically harsh etching step. This has been solved by the development of a double replication process. First, a mesoporous carbon matrix is prepared within the initial silica structure. In a second step, the carbon matrix is then used as a mold for the metal oxide precursor and removed by pyrolysis, thus allowing the synthesis of mesoporous ZrO_2, ZnO, or TiO_2 [93].

In addition to silica, aluminium metal is known to grow nanoporous oxides when anodized in acidic conditions and thus serve as a mold platform. As described in [99], highly ordered porous alumina is obtained by anodizing Al sheets in acidic conditions, typically using H_3PO_4 and $H_2C_2O_4$. By varying the anodizing conditions, the electrolyte temperature, the anodizing voltage, and/or the nano-texture of the aluminium substrate, the diameter, length, and the density of the parallel nanopores can be tuned in the ranges, respectively, ~10–300 nm, ~300 nm to 100 μm, and ~5×10^9 to 10^{11} pores/cm^2 [100].

4.5 Bottom-up and top-down synthesis of quasi-1D-structures

Inspired by the rapidly growing field of carbon nanotubes (CNT) with their exceptional properties, synthesis methods to prepare quasi-1D metal oxide nanostructrures have been investigated in the literature [101]. In contrast to CNT, whose properties strongly depend on chirality (difficult to control during synthesis), the composition and electronic properties of these structures can be controlled during the growth process [102]. During the past decade, numerous quasi-one-dimensional oxide nanostructures with useful functionalities, compositions, and morphologies have been prepared (cf. [100, 103, 104] and references therein). Figure 13 diagrammatically summarizes some of these novel nanogeometries including nanofibers, wires, belts, tubes, and heterostructures.

Several research groups have directed their attention to the preparation and characterization of metal oxide nanofibers for gas sensing [104–108], with some authors predicting gas sensing to be one of the first commercial application for 1D nanosystems [103]. Due to their large surface-to-volume ratio, such nanostructures offer excellent potential for conductometric gas sensors, since the sensing effect in these devices is largely attributed to heterogeneous catalytic reactions or adsorption processes at the sensor surface and space charge generation extending from the surface inwards as explained in Sec. 1. In addition, nanowires are easily configurable as field-effect transistors (FETs) with the position of the Fermi level within the nanowire varied to electronically control surface processes [100].

In general, one-dimensional nanostructures are synthesized by promoting the crystallization of solid-state structures along one direction, achievable by various techniques. These include the use of templates or capping agents, self-assembly, or growth of intrinsically anisotropic structures. To date, a great number of papers have been published in the active field of nanowire growth. Many excellent reviews are available summarizing the various manufacturing methods for nanowires and other quasi-1D structures [101, 103, 109]. In the following, we focus on bottom-up

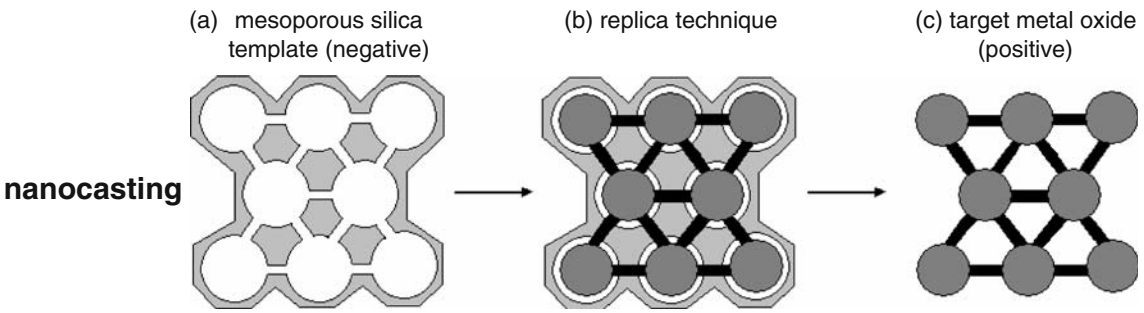

Fig. 12 Schematic representation of nanocasting with rigid matrices. For details see text

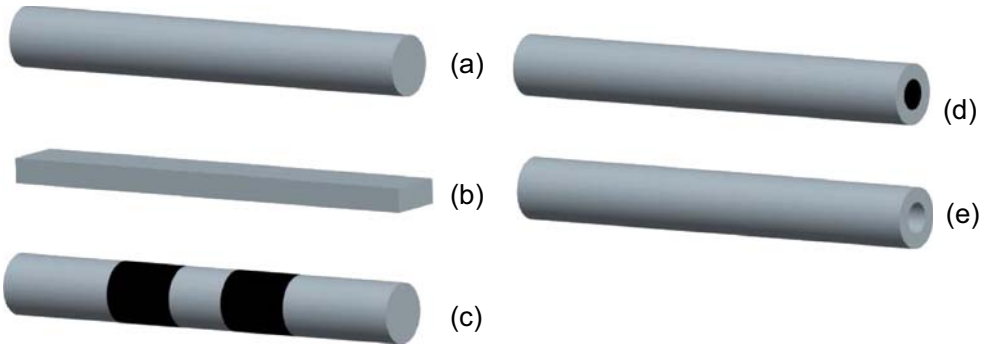

Fig. 13 Various types of quasi-1D nanostructures: Nanowires or -fibers (**a**), nanotapes or -belts (**b**), longitudinal heterostructures (**c**), coaxial heterostructures (**d**), and nanotubes (**e**)

gas-phase synthesis, i.e., the vapor–liquid–solid (VLS) and vapor–solid (VS) processes, with which most high-quality one-dimensional structures and ordered arrays are now grown. As novel top-down techniques, nano-carving and anodization of titania, which have been explicitly investigated for gas sensing, are also discussed.

4.5.1 Bottom-up: gas phase synthesis

The vapor–liquid–solid (VLS) mechanism, first reported in 1964 [110] and later rediscovered by various research groups [111–113], was shown to generate nanowires and nanorods from a rich variety of materials. In VLS growth, nanosized liquid metal droplets serve as seeds and templates for the one-dimensional growth from the gas phase containing the precursor reactant for wire formation. This reactant dissolves into the liquid droplet up to the saturation limit, nucleates, and eventually grows in the direction dictated by the droplets, which remain on top of the growing nanostructure. While the preparation of gas phase precursors is similar to the techniques used for thin-film growth (e.g., chemical vapor deposition, sputtering, or molecular beam epitaxy), the concentration of gaseous reactants, pressure, temperature, and flow rate must be carefully controlled to ensure homogeneous nanowire growth and to prevent secondary nucleation. A diagram of the VLS synthesis is shown in Fig. 14.

A crucial parameter in VLS growth is the choice of an appropriate metal catalyst which must be able to dissolve the target material and form a liquid alloy. Since the size of the catalyst droplets remains essentially unchanged during the entire growth process, lateral growth of an individual wire does not occur. Hence, the resulting nanowires are typically single crystalline with remarkable uniformity in diameter, usually on the order of 10 nm, over a length scale of >1 μm [103]. In general, the final fiber length can be modified via the growth time.

The VLS method is also the basis for synthesizing either longitudinal (Fig. 13(c)) or coaxial (Fig. 13(d)) nanowire heterostructures, which are useful both from a technical and a theoretical point of view. The first structure group involves switching between different vapor precursor supplies in mid-growth. Coaxial heterostructures, on the other hand, are obtained by coating a finalized array of nanowires with a uniform layer of a second material.

An alternative growth mechanism from the vapor phase has been reported for metal oxides, e.g., SnO_2, In_2O_3, or ZnO [113–116]. In this case, nano-ribbons with homogeneous cross sections ranging from 30 nm to 300 nm were grown by evaporating metal oxide powders without the presence of a liquid metal catalyst. Hence, this synthesis approach is called vapor–solid (VS) growth. While the actual growth mechanism is not yet fully understood, either intrinsically anisotropic or defect assisted directed growth are likely explanations. In 2002, Comini et al. reported conductometric SnO_2 nano-belt gas sensors prepared by vapor phase synthesis [117]. For electrical measurements, the nanobelts were transferred onto transducers equipped with sputtered platinum interdigitated electrodes. The analyte gases were CO, NO_2, and ethanol. Typical *n*-type semiconductor response was observed, i.e. an increase in conductivity upon CO and ethanol exposure and the opposite behaviour for NO_2. The same group also investigated the impact of fiber mesh density on sensitivity [118] and showed that the conductance of the layers, as well as the CO and NO_2 responses, increased with the density of the nano-belts.

Law et al. [106, 119] prepared SnO_2 nano-ribbons for photochemical, UV assisted NO_x sensing. Yu and coworkers successfully integrated tin oxide nano-belts with low-power microheaters for detecting dimethyl methylphosphonate (DMMP). They used an electric field-directed assembly method to trap and align the belts from a solution on top of electrode structures [120]. In this method, known as positive dielectrophoresis, microdevices equipped with two Pt electrodes were connected to an ac voltage source. After dispersing a solution containing the nanobelts on the device surface, the frequency of the ac field was adjusted to polarize the nanobelts, thus generating an attractive force. In an alternative approach adopted by Meier et al. [121], individual SnO_2 nanowires were electrostatically picked up with a dielectric microfiber, then

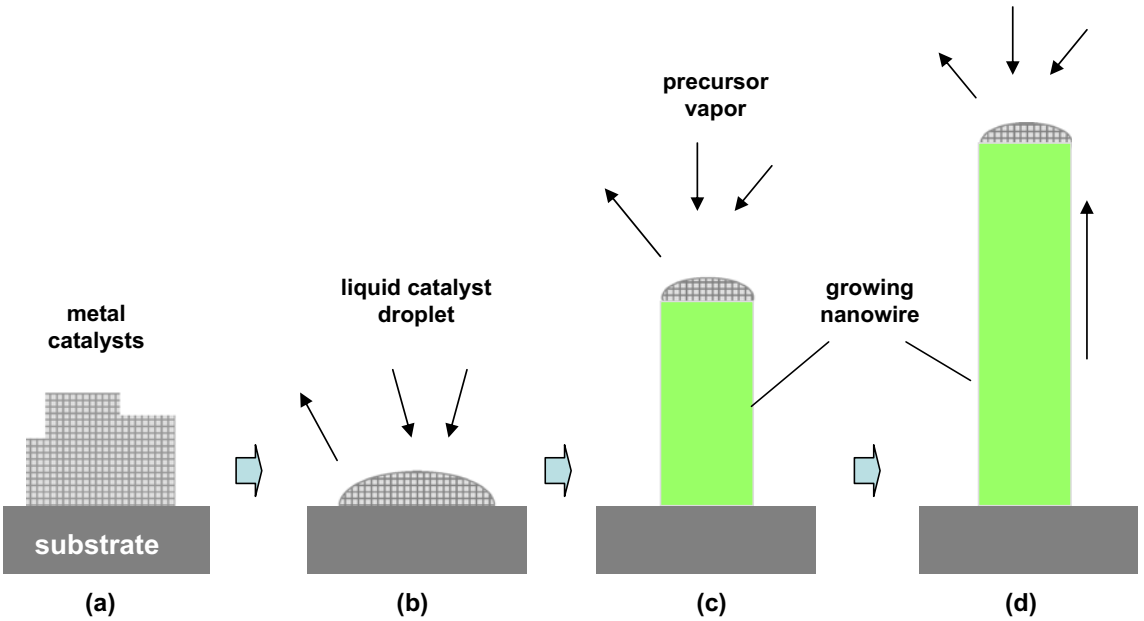

Fig. 14 VLS growth: After depositing a metal catalyst seed (**a**), the substrate is heated to high temperatures above the liquidus temperature of the metal (**b**). As described in the text, the target precursor is provided in form of a vapor. It dissolves into the liquid metal, nucleates, and grows to form a nanowire (**c** and **d**)

transferred to the microdevices, and oriented to make contact with the contact pads.

In [122], Zhang and coworkers reported the detection of NO_2 with In_2O_3 nanowire transistors operating at room temperature and achieved excellent performance with a detection limit as low as 20 ppb. Sysoev et al. [123] discussed initial steps towards a nanoscopic electronic nose based on the integration of a variety of oxide nanofibers in a single device. They combined SnO_2, TiO_2, and In_2O_3 nanowires on a commercial $Si:SiO_2$ wafer. By examining the responses from the three types of nanowires, they were able to discriminate between H_2 and CO.

4.5.2 Top-down

In addition to the bottom-up nanofiber synthesis discussed above, top-down approaches for the preparation of metal oxide quasi-1D structures have also been developed. As a simple, highly scalable, and low-cost technique to produce metal oxide nanofibers devices by a one-step gas phase reaction, a selective anisotropic etching process called *nanocarving* has been developed by Akbar and coworkers [124]. In this method, dense bulk metal oxide specimens are first produced by a conventional sintering step. The compacts are then exposed to flowing H_2/N_2 mixtures at elevated temperatures, yielding aligned fiber arrays with 15 to 50 nm diameters (cf. Fig. 15). The process was first developed for titania and later transferred to SnO_2-TiO_2 composites [125]. According to [126], the anisotropic etching proceeds with a parabolic rate law according to the following chemical reaction between hydrogen and TiO_2

$$TiO_2 + x\,H_2 \rightarrow TiO_{2-x} + x\,H_2O\,. \quad (8)$$

In addition to treatment with H_2/N_2 mixtures, the use of CO/CO_2 mixtures was also investigated for MoO_3 films [126]. By texturing the films in CO/CO_2 atmospheres, a porous microstucture with sub-micron pore diameters was obtained, attributed to phase changes and corresponding volume changes during treatment. The thus prepared films exhibited improved sensitivity and reduced response times compared with the untreated films.

As in the case of anodized aluminum foils, discussed as a potential mold for structure replication in Section 3.2, titanium metal is also known to grow well-defined porous structures when anodized in acidic media. In contrast to the porous alumina bodies, these structures may serve directly as gas sensitive devices. The Egashira group investigated planar array sensors based on titania nanotubules [127]. Arrays of parallel titania nanotubules with diameters in the range 20–100 nm were obtained by anodizing Ti foil in a hydrofluoric acid solution. Similar growth techniques were also investigated by Grimes and coworkers [128, 129]. Figure 16 presents corresponding structures and results of gas response measurements. The nanotube sensors exhibited a resistance change over several orders of magnitude in the presence of 100 ppm hydrogen at room temperature while demonstrating complete reversibility, repeatability, high selectivity, negligible drift and wide dynamic range.

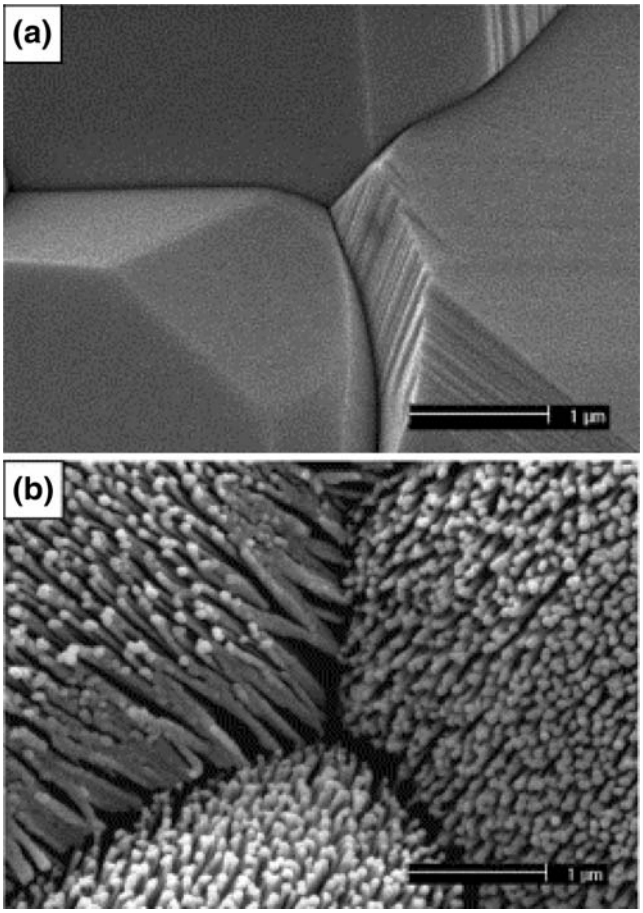

Fig. 15 Nanocarved TiO_2 structures: SEM micrographs after sintering at 1200°C in air (**a**) and after exposure to H_2/N_2 mixtures at 700°C (**b**). Reprinted from [124], with permission from Elsevier

4.6 Electric field assisted methods

Electric field assisted methods such as electrospinning or electrospraying rely on electric forces for film deposition. The operational principles of each of these methodsare similar. A high voltage, in the kV range, is applied between a substrate and the needle of a syringe, which contains the precursor solution and is operated at a constant delivery rate, e.g., by a programmable syringe pump. When the electric field is sufficient to overcome the surface tension of the fluid, a jet forms, and a thin film is deposited on the substrate. Its morphology is governed by several parameters such as deposition rate, voltage, and distance between substrate and needle. After drying, the deposited film is heat-treated. As an alternative, in-situ deposition on a heated substrate can be conducted.

In the case of electrospraying, the liquid precursor contains unreacted solvated components of the metal oxide film. For electrospinning, however, an appropriate polymer solution is added. An important feature is the choice of an effective, highly volatile solvent, which evaporates in-situ. Appropriate systems are polyvinylpyrollidone (PVP) in ethanol or cellulose acetate (CA) in acetone. Under the action of the electric field, a fine polymer fiber network forms, which encapsulates the metal oxide precursor. This polymer matrix is removed subsequently during an appropriate thermal treatment. Ceramic nano-wires remain on the substrate.

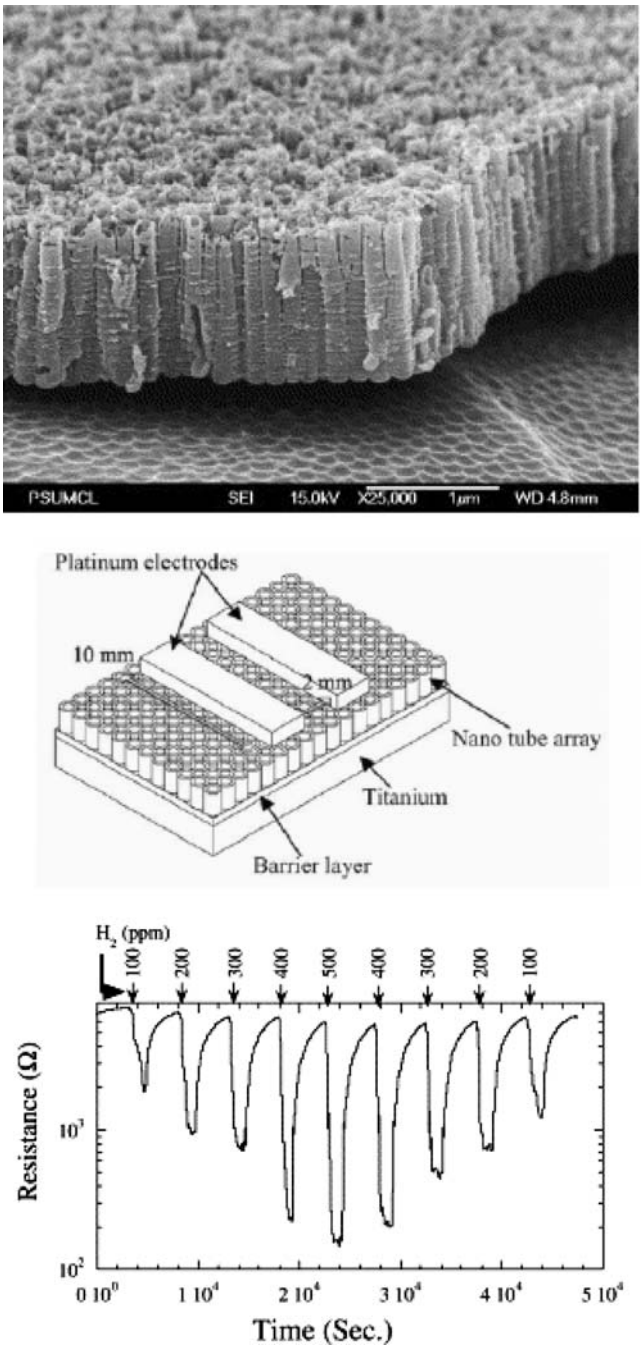

Fig. 16 TiO_2 nanotubules. *Left*: SEM images showing the topology of anodized Ti samples. Reprinted from [129], with permission from Elsevier. *Right*: corresponding planar sensor set-up and sensing performance towards hydrogen at 290°C. Reprinted from [130], with permission from Elsevier

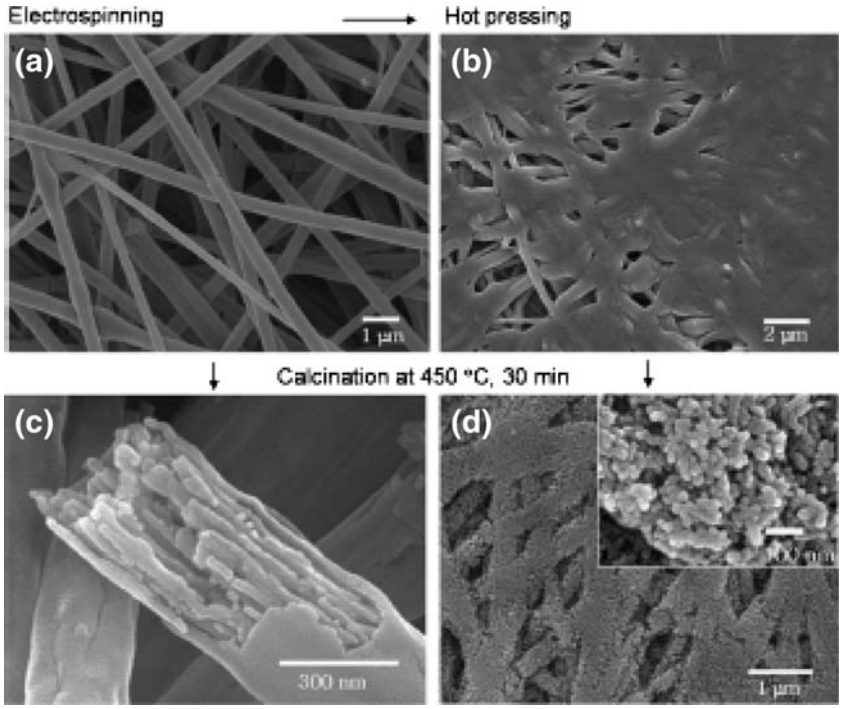

Fig. 17 Electrospinning and hot-pressing of metal oxide materials. Reprinted with permission from [135]. Copyright (2006) American Chemical Society. (**a**) SEM image of the as-spun metal oxide-polymer composite, (**b**) composite after hot-pressing at 120°C, (**c**) unpressed fibers after calcinations at 450°C, (**d**) hot-pressed fibers after calcinations. For details see text

The main advantage of electrospraying is that the particle size of a film is reduced to a nanometer-scale due to the fact that the film is deposited from a precursor in an aerosol form. This is of great interest in the case of conductometric sensors where small particle sizes are required. In addition, electrospraying presents a simple set-up, high-deposition efficiency, ambient-atmosphere operation, large choice of precursors, and ready control of surface morphology and film composition [131].

Matsushima et al. [132] investigated electrosprayed tin oxide thin films. The films were characterized by SE and

Table 1 Summary of the advantages and limitations of the novel deposition methods with respect to potential applications in metal oxide gas sensing.

Method	Advantages	Limitations
Soft lithography	Feature resolutions down to 1 μm Simple and versatile patterning of molds	Drying conditions need to be carefully controlled Complex optimization of the precursor systems required
Direct writing		
MAPLE	Direct patterning with feature resolution down to 10 μm Suitable for a broad variety of materials including nanosized precursors	Limited to 2D, low aspect ratios
Ink-jet	Versatile direct patterning tool Potential for use in high throughput materials discovery	Limited to 2D Ink optimization is complex
3D-printing	Versatile tool to access 3D-patterns Line widths <1 μm can be achieved	Ink optimization is complex Not yet available for many materials systems
In-situ spraying	Simple, inexpensive multilayer deposition Homogeneous films	Limited to films (no direct patterning)
Structure replication	Synthesis of high surface area materials	For many metal oxides: two-step process (template of silica matrix + nanocasting) required
Nanofiber growth	Very high surface-to-volume ratio	Single nanofibers: limited reproducibility Difficult to assemble into real-world devices
Nanocarving	Well-defined nanostructured devices with high surface area	Available only for a limited number of materials
Electric field assisted methods		
Electrospinning	Simple set-up operating under ambient-atmosphere Unoriented, porous fiber mats with high surface areas	Without additional treatment: poor adhesion to substrate
Electrospraying	Simple set-up operating under ambient-atmosphere Preparation of films with nanoscaled features	Deposition parameters need to be carefully controlled

found to be composed of particles in the range from 100 to 200 nm. The layer thickness increased linearly with spray time. In hydrogen response tests, a notable response towards the analyte was observed, although not as responsive as thin films prepared by the ion-beam sputtering method. Ghimbeu et al. [133] studied the use of electrospraying tungsten oxide with particular focus on the effect of deposition temperature on film morphology, microstructure and electrical properties. The films deposited at low substrate temperatures (200°C to 300°C) were dense and exhibited good adhesion. At higher substrate temperatures (400°C), however, porous films with poor adhesion were obtained. This was attributed to complete solvent evaporation at high temperature before arriving at the substrate surface.

The use of electrospinning to deposit nanomaterials was reported by Reneker in 1996 and first applied to form polymeric nanofibers [134]. On the substrate, unoriented fiber mats as shown exemplarily in Fig. 17(a) are obtained. Later, the method was transferred to prepare oxide nanofibers, which are either formed directly as discussed above by spinning a suitable sol–gel precursor [107, 136], or by coating polymer fiber networks [137].

While the quasi-1D structures presented in the previous section show excellent potential as gas sensors due to their high surface-to-volume ratio, reproducibility of the single fiber arrays is very difficult to achieve. In this regard, the application of unoriented fiber mats, instead of individual fibers, may enhance device performance. To solve the problem of poor adhesion between fiber mats and the substrate, Kim et al. introduced an additional hot-pressing step after titania fiber deposition [135]. Besides improving adhesion, this treatment was found to have an impact on the microstructure of the fibers as shown in Fig. 17. The as-spun metal oxide-polymer composite fibers exhibit a range of diameters from 200 to 500 nm (Fig. 17(a)). When calcined without hot-pressing to remove the organic vehicle, a bundle structure composed of sheaths of 200–500 nm diameters was obtained. In some cases, the outer sheaths were broken revealing cores filled with ~10 nm thick fibrils as shown in Fig. 17(c). By introducing the hot-pressing step prior to calcination, an interconnected morphology of the TiO_2/polymer composite fibers was obtained, as illustrated in Fig. 17(b), due to the partial melting of the polymer vehicle. Subsequent calcination resulted in the exceptionally high surface area structures shown in Fig. 17(d). The mechanical pressure applied during the hot pressing served to break the outer sheaths thereby exposing the fibrils and leading to an exceptionally high surface-to-volume ratio. The hot-pressed TiO_2 fiber sensors exhibited improved NO_x characteristics with detection limits down to the ppb range [135]. The combined hot-pressing/electrospinning technique was successfully transferred to SnO_2 and SnO_2-TiO_2 composites (Kim, in preparation).

While mainly used for "simple" oxides such as WO_3, SnO_2, or TiO_2 [107, 135, 138] electrospinning was also applied to more complex compounds. By side-by-side electrospinning, Liu et al. [139] prepared SnO_2/TiO_2 composite nanofibers, a materials system which is also of interest for gas sensing [125, 140]. Sahner et al. reported hydrocarbon sensors of electrospun ternary $SrTi_{0.8}Fe_{0.2}O_{3-\delta}$ perovskites with improved sensor characteristics compared to conventional devices obtained by screen-printing of micro-scaled powders [141].

5 Conclusion

The development of novel deposition techniques is an extremely active research field. In the scope of metal oxide gas sensors, a large variety of promising methods has been introduced within the past decade. Table 1 summarizes the potential advantages and current limitations of these techniques with respect to their potential application in the preparation of metal oxide-based gas sensors.

Compared to the well-established deposition tools, namely screen-printing, PVD, CVD, or sol–gel deposition, these novel approaches are designed either to improve micro- and nanostructure control of the films, or to introduce direct-patterning features to reduce the need for cost- and time-intensive post processing. Both advantages are crucial for further optimization of gas sensitive devices and eventually to meet the requirements of high sensitivity, selectivity, and stability at low manufacturing costs.

Acknowledgments K. Sahner gratefully acknowledges financial support of the Bavarian Science Foundation, Germany (Grant PDOK 29/05) and H. Tuller the National Science Foundation under Grants DMR 0243993 and ECS 0428696.

References

1. A.M. Azad, S.A. Akbar, S.G. Mhaisalkar, L.D. Birkefeld, K.S. Goto, Solid-state gas sensors: a review J. Electrochem. Soc **139**, 3690–3704 (1992). doi:10.1149/1.2069145
2. F. Rettig, R. Moos, Direct thermoelectric hydrocarbon gas sensors based on SnO_2 IEEE Sens. J **7**, 1490–1496 (2007). doi:10.1109/JSEN.2007.906887
3. F. Rettig, R. Moos, Direct thermoelectric gas sensors: design aspects and first gas sensors Sens. Actuators B Chem **123**, 413–419 (2007). doi:10.1016/j.snb.2006.09.002
4. M. Nishibori, W. Shin, K. Tajima, L.F. Houlet, N. Izu, T. Itoh, S. Tsubota, I. Matsubara, Thermoelectric gas sensor using Au loaded titania CO oxidation catalyst J. Ceram. Soc. Jpn **115**, 37–41 (2007). doi:10.2109/jcersj.115.37
5. M. Law, D.J. Sirbuly, P.D. Yang, Chemical sensing with nanowires using electrical and optical detection Int. J. Nanotechnology **4**, 252–262 (2007). doi:10.1504/IJNT.2007.013472
6. S. Okazaki, H. Nakagawa, S. Asakura, Y. Tomiuchi, N. Tsuji, H. Murayama, M. Washiya, Sensing characteristics of an optical

fiber sensor for hydrogen leak Sens. Actuators B Chem **93**, 142–147 (2003). doi:10.1016/S0925-4005(03)00211-9
7. H.L. Tuller, Review of electrical properties of metal oxides as applied to temperature and chemical sensing Sens. Actuators **4**, 679–688 (1984). doi:10.1016/0250-6874(83)85082-3
8. J. Daniels, K.H. Härdtl, D. Hennings, Defect chemistry and electrical conductivity of doped barium titanate ceramics: I–III Philips Res. Rep **31**, 489–525 (1976)
9. J.W. Fergus, Doping and defect association in oxides for use in oxygen sensors J. Mater. Sci **38**, 4259–4270 (2003). doi:10.1023/A:1026318712367
10. J.W. Fergus, Perovskite oxides for semiconductor-based gas sensors Sens. Actuators B Chem **123**, 1169–1179 (2007). doi:10.1016/j.snb.2006.10.051
11. J. Gerblinger, M. Meixner, Influence of dopants on the response time and the signals of lambda sensors based on thin films of strontium titanate Sens. Actuators B Chem **6**, 231–235 (1992). doi:10.1016/0925-4005(92)80061-2
12. R. Moos, W. Menesklou, H. Schreiner, K.H. Härdtl, Materials for temperature independent resistive oxygen sensors for combustion exhaust gas control Sens. Actuators B Chem **67**, 178–183 (2000). doi:10.1016/S0925-4005(00)00421-4
13. K. Sahner, R. Moos, Modeling of hydrocarbon sensors based on p-type semiconducting perovskites Phys. Chem. Chem. Phys **9**, 635–642 (2007). doi:10.1039/b612965j
14. G. Heiland, Zum Einfluss von Wasserstoff auf die elektrische Leitfahigkeit an der Oberflache von Zinkoxydkristallen (On the effect of hydrogen on the electrical conductivity at the surface of tin oxide crystals) Z. Phys **148**(1), 15–27 (1957). doi:10.1007/BF01327362
15. T. Seiyama, A. Kato, K. Fujiishi, M. Nagatani, A new detector for gaseous components using semiconductive thin films Anal. Chem **34**, 1502 (1962). doi:10.1021/ac60191a001
16. N. Taguchi, U.S. Patent 3,631,436 (1971)
17. G. Eranna, B. Joshi, D. Runthala, R. Gupta, Oxide materials for development of integrated gas sensors—a comprehensive review Crit. Rev. Solid State Mater. Sci **29**, 111–188 (2004). doi:10.1080/10408430490888977
18. G. Korotcenkov, Metal oxides for solid-state gas sensors: what determines our choice Mater. Sci. Eng. B—Solid State Mater. Adv. Technol **139**, 1–23 (2007)
19. D. Williams, in Conduction and gas response of semiconductor gas sensors, ed. by Moseley, P., Tofield, B. *Solid State Gas Sensors*, *The Adam Hilger Series on Sensors* (IOP, Bristol, 1987), pp. 71–123
20. W. Göpel, J. Hesse, J.N. Zemel, *Sensors* (Wiley-VCH, Weinheim, 1995)
21. N. Barsan, M. Schweizer-Berberich, W. Göpel, Fundamental and practical aspects in the design of nanoscaled SnO_2 gas sensors: a status report Fresenius J. Anal. Chem **365**, 287–304 (1999). doi:10.1007/s002160051490
22. M. Batzill, Surface science studies of gas sensing materials: SnO_2 Sensors **6**, 1345–1376 (2006)
23. A. Gurlo, Interplay between O_2 and Sn O_2: oxygen ionosorption and spectroscopic evidence for adsorbed oxygen ChemPhysChem **7**, 2041–2052 (2006). doi:10.1002/cphc.200600292
24. T. Wolkenstein, *Electronic Processes on Semiconductor Surfaces During Chemisorption* (Consultants Bureau, New York, 1991)
25. A. Rothschild, Y. Komem, Numerical computation of chemisorption isotherms for device modeling of semiconductor gas sensors Sens. Actuators B Chem **93**, 362–369 (2003). doi:10.1016/S0925-4005(03)00212-0
26. A. Rothschild, Y. Komem, N. Ashkenasy, Quantitative evaluation of chemisorption processes on semiconductors J. Appl. Phys **92**, 7090–7097 (2002). doi:10.1063/1.1519946
27. R. Hagenbeck, R. Waser, Influence of temperature and interface charge on the grain boundary conductivity in acceptor-doped $SrTiO_3$ ceramics J. Appl. Phys **83**, 2083–2092 (1998). doi:10.1063/1.366941
28. T. Baiatu, R. Waser, K. Härdtl, dc electrical degradation of perovskite-type titanates: III, a model of the mechanism J. Am. Ceram. Soc. **73**, 1663–1673 (1990). doi:10.1111/j.1151-2916.1990.tb09811.x
29. N. Barsan, U. Weimar, Conduction model of metal oxide gas sensors J. Electroceram **7**, 143–167 (2001). doi:10.1023/A:1014405811371
30. N. Barsan, U. Weimar, Understanding the fundamental principles of metal oxide based gas sensors; the example of CO sensing with SnO_2 sensing in the presence of humidity J. Phys. Condens. Matter **15**, R813–R839 (2003). doi:10.1088/0953-8984/15/20/201
31. C.O. Park, S.A. Akbar, Ceramics for chemical sensing J. Mater. Sci **38**, 4611–4637 (2003). doi:10.1023/A:1027402430153
32. M.E. Franke, T.J. Koplin, U. Simon, Metal and metal oxide nanoparticles in chemiresistors: does the nanoscale matter Small **2**, 36–50 (2006). doi:10.1002/smll.200500261
33. G. Korotchenkov, Gas response control through structural and chemical modification of metal oxide films: state of the art and approaches Sens. Actuators B Chem **107**, 202–232 (2005). doi:10.1016/j.snb.2004.11.097
34. N. Yamazoe, G. Sakai, K. Shimanoe, Oxide semiconductor gas sensors Catal. Surv. Asia **7**, 63–75 (2003). doi:10.1023/A:1023436725457
35. S. Ahlers, G. Müller, T. Doll, in Factors influencing the gas sensitivity of metal oxide materials, ed. by C. Grimes, E. Dickey, M. Pishko. *Encyclopedia of Sensors*, vol. X (American Scientific, Stevenson Ranch, CA, 2006), pp. 1–35
36. G. Sakai, N. Matsunaga, K. Shimanoe, N. Yamazoe, Theory of gas-diffusion controlled sensitivity for thin film semiconductor gas sensor Sens. Actuators B Chem **80**, 125–131 (2001). doi:10.1016/S0925-4005(01)00890-5
37. C.O. Park, S.A. Akbar, W. Weppner, Ceramic electrolytes and electrochemical sensors J. Mater. Sci **38**, 4639–4660 (2003). doi:10.1023/A:1027454414224
38. J.W. Fergus, Solid electrolyte based sensors for the measurement of CO and hydrocarbon gases Sens. Actuators B Chem **122**, 683–693 (2007). doi:10.1016/j.snb.2006.06.024
39. M. Holzinger, J. Maier, W. Sitte, Fast CO_2-selective potentiometric sensor with open reference electrode Solid State Ion **86–88**, 1055–1062 (1996). doi:10.1016/0167-2738(96)00250-0
40. T. Kida, Y. Miyachi, K. Shimanoe, N. Yamazoe, NASICON thick film-based CO2 sensor prepared by a sol–gel method Sens. Actuators B Chem **80**, 28–32 (2001). doi:10.1016/S0925-4005(01)00878-4
41. C.M. Mari, G. Terzaghi, M. Bertolini, G.B. Barbi, A chlorine gas potentiometric sensor Sens. Actuators B Chem **8**, 41–45 (1992). doi:10.1016/0925-4005(92)85006-I
42. D. Lutic, M. Strand, A. Lloyd-Spetz, K. Buchholt, E. Eliana Ieva, P. Käll, M. Sanati, Catalytic properties of oxide nanoparticles applied in gas sensors Top. Catal **45**, 105–109 (2007). doi:10.1007/s11244-007-0248-1
43. A. Sammn, S. Gebremariam, L. Rimai, X. Zhang, J. Hangas, G. W . Auner, J. Appl. Phys **87**, 3101 (2000). doi:10.1063/1.372305
44. A. Lloyd Spetz, L. Uneus, H. Svenningstorp, P. Tobias, L.G. Ekedahl, O. Larsson, A. Göras, S. Savage, C. Harris, P. Martensson, R. Wigren, P. Salomonsson, B. Häggendahl, P. Ljung, M. Mattsson, I. Lundström, SiC based field effect gas sensors for industrial applications Phys. Stat. Sol. (A) **185**, 15–25 (2001)
45. C.K. Kim, J.H. Lee, Y.H. Lee, N.I. Cho, D.J. Kim, W.P. Kang, Hydrogen sensing characteristics of Pd-SiC Schottky diode operating at high temperature J. Electron. Mater **28**, 202–205 (1999). doi:10.1007/s11664-999-0014-1

46. A. Vasiliev, W. Moritz, V. Fillipov, L. Bartholomäus, A. Terentjev, T. Gabusjan, Sens. Actuators B Chem **49**, 133 (1998). doi:10.1016/S0925-4005(98)00041-0
47. L.-G. Ekedahl, M. Eriksson, I. Lundström, Acc. Chem. Res **31**, 249 (1998). doi:10.1021/ar970068s
48. V. Mecea, Is quartz crystal microbalance really a mass sensor Sens. Actuators A Phys **128**, 270–277 (2006). doi:10.1016/j.sna.2006.01.023
49. I. Simon, N. Barsan, M. Bauer, U. Weimar, Micromachined metal oxide gas sensors: opportunities to improve sensor performance Sens. Actuators B Chem **73**, 1–26 (2001). doi:10.1016/S0925-4005(00)00639-0
50. M. Graf, A. Gurlo, N. Barsan, U. Weimar, A. Hierlemann, Microfabricated gas sensor systems with sensitive nanocrystalline metal-oxide films J. Nanopart. Res **8**, 823–839 (2006). doi:10.1007/s11051-005-9036-7
51. K.D. Benkstein, C.J. Martinez, G. Li, D.C. Meier, C.B. Montgomery, S. Semancik, Integration of nanostructured materials with MEMS microhotplate platforms to enhance chemical sensor performance J. Nanopart. Res **8**, 809–822 (2006). doi:10.1007/s11051-005-9019-8
52. A. Kumar, G.M. Whitesides, Features of gold having micrometer to centimetre dimensions can be formed through a combination of stamping with an elastomeric stamp and an alkanethiol ink followed by chemical etching Appl. Phys. Lett **63**, 2002–2004 (1993). doi:10.1063/1.110628
53. M. Heule, Shaping ceramics in small scale—from microcomponents to gas sensors, Ph.D. thesis, ETH Zürich (2003)
54. M. Heule, U.P. Schonholzer, L.J. Gauckler, Patterning colloidal suspensions by selective wetting of microcontact-printed surfaces J. Am. Ceram. Soc **24**, 2733–2739 (2004). doi:10.1016/j.jeurceramsoc.2003.09.011
55. H.J. Lim, D.Y. Lee, Y.J. Oh, Gas sensing properties of ZnO thin films prepared by microcontact printing Sens. Actuators A Phys **125**, 405–410 (2006). doi:10.1016/j.sna.2005.08.031
56. M. Heule, L.J. Gauckler, Miniaturised arrays of tin oxide gas sensors on single microhotplate substrates fabricated by micromolding in capillaries Sens. Actuators B Chem **93**, 100–106 (2003). doi:10.1016/S0925-4005(03)00243-0
57. S.J. Ahn, J. Moon, Vacuum-assisted microfluidic lithography of ceramic microstructures J. Am. Ceram. Soc **88**, 1171–1174 (2005). doi:10.1111/j.1551-2916.2005.00329.x
58. D.B. Chrisey, Materials Processing: The power of direct writing Science **289**, 879–881 (2000). doi:10.1126/science.289.5481.879
59. R. Rella, J. Spadavecchia, M.G. Manera, S. Capone, A. Taurino, M. Martino, A.P. Caricato, T. Tunno, Acetone and ethanol solid-state gas sensors based on TiO_2 nanoparticles thin film deposited by matrix assisted pulsed laser evaporation Sens. Actuators B Chem **127**, 426–431 (2007). doi:10.1016/j.snb.2007.04.048
60. C.B. Arnold, P. Serra, A. Piqué, Laser direct-write techniques for printing of complex materials MRS Bull **32**, 23–31 (2007)
61. R. Fryček, M. Jel, nek, T. Kocourek, P. Ftil, M. Vrňata, V. Myslík, M. Vrbová, Thin organic Layers prepared by MAPLE for gas sensor application Thin Solid Films **495**, 308–311 (2006). doi:10.1016/j.tsf.2005.08.178
62. J. Evans, M. Edirisinghe, P.V. Coveney, J. Eames, Combinatorial searches of inorganic materials using the ink jet printer: science, philosophy and technology J. Eur. Ceram. Soc **21**, 2291–2299 (2001). doi:10.1016/S0955-2219(01)00289-8
63. J. Evans, Direct ink jet printing of ceramics: experiment in teleology Br. Ceram. Trans. **100** (2001). doi:10.1179/096797801681332
64. M. Bale, J.C. Carter, C.J. Creighton, H.J. Gregory, P.H. Lyon, P. Ng, L. Webb, A. Wehrum, Ink-jet printing: The route to production of full-color P-OLED displays J. Soc. Inf. Disp **14**, 453–459 (2006). doi:10.1889/1.2206109
65. D. Kim, S. Jeong, S. Lee, B.K. Parka, J. Moon, Organic thin film transistor using silver electrodes by the ink-jet printing technology Thin Solid Films **515**, 7692–7696 (2007). doi:10.1016/j.tsf.2006.11.141
66. M.M. Mohebi, J.R.G. Evans, Combinatorial ink-jet printer for ceramics: Calibration J. Am. Ceram. Soc. **86**, 1654–1661 (2003)
67. J. Wang, M. Mohebi, J. Evans, Two methods to generate multiple compositions in combinatorial ink-jet printing of ceramics Macromol. Rapid Commun **26**, 304–309 (2005). doi:10.1002/marc.200400460
68. J. Wang, J.R. Evans, Library preparation using an aspirating-dispensing ink-jet printer for combinatorial studies in ceramics J. Mater. Res **20**, 2733–2740 (2005). doi:10.1557/JMR.2005.0348
69. S. Okamura, R. Takeuchi, T. Shiosaki, Fabrication of ferroelectric Pb(ZrTi)O3 thin films with various Zr/Ti ratios by ink-jet printing Jpn. J. Appl. Phys **41**, 6714–6717 (2002). doi:10.1143/JJAP.41.6714
70. J. Rossiny, S. Fearn, J. Kilner, Y. Zhang, L. Chen, Combinatorial searching for novel mixed conductors Solid State Ion **177**, 1789–1794 (2006). doi:10.1016/j.ssi.2006.02.050
71. W. Shen, Y. Zhao, C. Zhang, The preparation of ZnO based gas-sensing thin films by ink-jet printing method Thin Solid Films **483**, 382–387 (2005). doi:10.1016/j.tsf.2005.01.015
72. D.H. Lee, Y.J. Chang, W. Stickle, C.H. Chang, Functional Porous Tin Oxide Thin Films Fabricated by Inkjet Printing Process Electrochem. Solid State Lett **10**, K51–K54 (2007). doi:10.1149/1.2773531
73. H. Seh, T. Hyodo, H.L. Tuller, Bulk acoustic wave resonator as a sensing platform for NOx at high temperatures Sens. Actuators B Chem **108**, 547–552 (2005). doi:10.1016/j.snb.2004.11.083
74. T. Hyodo, K. Sasahara, Y. Shimizu, M. Egashira, Preparation of macroporous SnO_2 films using PMMA microspheres and their sensing properties to NO_x and H_2 Sens. Actuators B Chem **106**, 580–590 (2005). doi:10.1016/j.snb.2004.07.024
75. J.E. Smay, J. Cersarano III, J.A. Lewis, Colloidal Inks for directed assembly of 3-D periodic structures Langmuir **18**, 5429–5437 (2002). doi:10.1021/la0257135
76. J.A. Lewis, Colloidal processing of ceramics J. Am. Ceram. Soc **83**, 2341–1359 (2000)
77. M. Heule, S.G.L.J. Vuillemin, Powder-based ceramic meso- and microscale fabrication processes Adv. Mater **15**, 1237–1245 (2003). doi:10.1002/adma.200300375
78. B.Y. Tay, J.R.G. Evans, M.J. Edirisinghe, Solid free form fabrication of ceramics Int. Mater. Rev **48**, 341 (2003). doi:10.1179/095066003225010263
79. Q. Li, J.A. Lewis, Nanoparticle inks for directed assembly of three-dimensional periodic structures Adv. Mater **15**, 1639–1643 (2003). doi:10.1002/adma.200305413
80. G.M. Gratson, J.A. Lewis, Phase behavior and rheological properties of polyelectrolyte inks for direct-write assembly Langmuir **21**, 457–464 (2005). doi:10.1021/la048228d
81. J.E. Smay, J. Cesarano III, B.A. Tuttle, J.A. Lewis, Directed Colloidal Assembly of Linear and Annular Lead Zirconate Titanate Arrays J. Am. Ceram. Soc **87**, 293–295 (2004). doi:10.1111/j.1551-2916.2004.00293.x
82. G.M. Gratson, F. García-Santamaría, V. Lousse, M. Xu, S. Fan, J.A. Lewis, P.V. Braun, Direct-write assembly of three-dimensional photonic ctystals: conversion of polymer scaffolds to silicon hollow-woodpile structures Adv. Mater **18**, 461–465 (2006). doi:10.1002/adma.200501447
83. E.B. Duoss, M. Twardowski, J.A. Lewis, Sol–Gel Inks for Direct-Write Assembly of Functional Oxides Adv. Mater **19**, 3485–3489 (2007)
84. R. Strobel, S. Pratsinis, Flame aerosol synthesis of smart nanostructured materials J. Mater. Chem **17**, 4743–4756 (2007). doi:10.1039/b711652g

85. Y. Liu, E. Koep, M.L. Liu, Highly sensitive and fast-responding SnO_2 sensor fabricated by combustion chemical vapor deposition Chem. Mater **17**, 3997–4000 (2005). doi:10.1021/cm050451o
86. L. Madler, T. Sahm, A. Gurlo, N. Barsan, J.D. Grunwald, U. Weimar, S.E. Pratsinis, Sensing low concentrations of CO using flame-spray-made Pt/SnO_2 nanoparticles J. Nanopart. Res **8**, 783–796 (2006). doi:10.1007/s11051-005-9029-6
87. T. Sahm, W. Rong, N. Barsan, L. Mädler, U. Weimar, Sensing of CH_4, CO and ethanol with in situ nanoparticle aerosol-fabricated multilayer sensors Sens. Actuators B Chem. **127**, 63–68 (2007). doi:10.1016/j.snb.2007.07.001
88. R. Strobel, F. Krumeich, W. Stark, S. Pratsinis, A. Baiker, Flame spray synthesis of Pd/Al_2O_3 catalysts and their behavior in enantioselective hydrogenation J. Catal. **222**, 307–314 (2004)
89. T. Sahm, L. Mädler, A. Gurlo, N. Barsan, S. Pratsinis, U. Weimar, Flame spray synthesis of tin dioxide nanoparticles for gas sensing Sens. Actuators B Chem **98**, 148–153 (2004). doi:10.1016/j.snb.2003.10.003
90. H. Herman, Thermal spray: Current status and future trends MRS Bull **25**, 17–25 (2000)
91. S. Sampath, Thermal-spray processing of materials MRS Bull **25**, 12–14 (2000)
92. K. Ahn, B.W. Wessels, S. Sampath, Spinel humidity sensors prepared by thermal spray direct writing Sens. Actuators B Chem **107**, 342–346 (2005). doi:10.1016/j.snb.2004.10.020
93. M. Tiemann, Porous metal oxides as gas sensors Chem. Eur. J **13**, 8376–8388 (2007). doi:10.1002/chem.200700927
94. G. Li, S. Kawi, High-surface-area SnO_2: a novel semiconductor-oxide gas sensor Mater. Lett **34**, 98–102 (1998)
95. Y. Shimizu, A. Ayami Jono, T. Takeo Hyodo, M. Egashira, Preparation of large mesoporous SnO_2 powder for gas sensor application Sensors Actuators B **108**, 56–61 (2005). doi:10.1016/j.snb.2004.10.047
96. A. Prim, E. Pellicer, E. Rossinyol, F. Peirp, A. Cornet, J.R. Morante, A novel mesoporous CaO-loaded In_2O_3 material for CO_2 sensing Adv. Funct. Mater **17**, 2957–2963 (2007). doi:10.1002/adfm.200601072
97. E. Rossinyol, A. Prim, E. Pellicer, J. Rodriguez, F. Peiro, A. Cornet, J.R. Morante, B.Z. Tian, T. Bo, D.Y. Zhao, Mesostructured pure and copper-catalyzed tungsten oxide for NO_2 detection Sens. Actuators B, Chemical **126**, 18–23 (2007)
98. E. Rossinyol, A. Prim, E. Pellicer, J. Arbiol, F. Hernandez–Ramirez, F. Peiro, A. Cornet, J.R. Morante, L.A. Solovyov, B.Z. Tian, T. Bo, D.Y. Zhao, Synthesis and characterization of chromium-doped mesoporous tungsten oxide for gas-sensing applications Adv. Funct. Mater. **17**, 1801–1806 (2007). doi:10.1002/adfm.200600722
99. F. Li, L. Zhang, R.M. Metzger, On the Growth of Highly Ordered Pores in Anodized Aluminum Oxide Chem. Mater **10**, 2470–2480 (1998). doi:10.1021/cm980163a
100. A. Kolmakov, M. Moskovits, Chemical sensing and catalysis by one-dimensional metal-oxide nanostructures Annu. Rev. Mater. Res. **34**, 151–180 (2004). doi:10.1146/annurev.matsci.34.040203.112141
101. J. Wang, S. Xie, W. Zhou, Growth of binary oxide nanowires MRS Bull **32**, 123–126 (2007)
102. C.M. Lieber, Z.L. Wang, Functional nanowires MRS Bull **32**, 99–108 (2007)
103. M. Law, J. Goldberger, P.D. Yang, Semiconductor nanowires and nanotubes Annu. Rev. Mater. Res **34**, 83–122 (2004). doi:10.1146/annurev.matsci.34.040203.112300
104. E. Comini, Metal oxide nano-crystals for gas sensing Anal. Chim. Acta **568**, 28–40 (2006). doi:10.1016/j.aca.2005.10.069
105. F. Patolsky, B.P. Timko, G. Zheng, C.M. Lieber, Nanowire-based nanoelectronic devices in the life sciences MRS Bull **32**, 142–149 (2007)
106. M. Law, H. Kind, B. Messer, F. Kim, P. Yang, Photochemical sensing of NO_2 with SnO_2 nanoribbon nanosensors at room temperature Angew. Chem. Int. Ed **41**, 2405–2408 (2002) doi:10.1002/1521-3773(20020703)41:13<2405::AID-ANIE2405>3.0.CO;2-3
107. P.I. Gouma, Nanostructured polymorphic oxides for advanced chemosensors Rev. Adv. Mater. Sci **5**, 147–154 (2003)
108. F. Hernandez-Ramirez, A. Tarancon, O. Casals, J. Rodriguez, A. Romano-Rodriguez, J.R. Morante, S. Barth, S. Mathur, T.Y. Choi, D. Poulikakos, V. Callegari, P.M. Nellen, Fabrication and electrical characterization of circuits based on individual tin oxide nanowires Nanotechnology **17**, 5577–5583 (2006). doi:10.1088/0957-4484/17/22/009
109. W. Lu, C.M. Lieber, Semiconductor nanowires J. Phys. D Appl. Phys **39**, R387–R406 (2006). doi:10.1088/0022-3727/39/21/R01
110. R.S. Wagner, W.C. Ellis, Vapor–liquid–solid mechanism of single crystal growth Appl. Phys. Lett **4**, 89–90 (1964). doi:10.1063/1.1753975
111. J. Westwater, D.P. Gosain, S. Tomiya, S. Usui, H. Ruda, Growth of silicon nanowires via gold/silane vapor–liquid–solid reaction J. Vac. Sci. Technol. B **15**, 554–557 (1997). doi:10.1116/1.589291
112. Y. Wu, P. Yang, Direct observation of vapor–liquid–solid nanowire growth J. Am. Chem. Soc. **123**, 3165–3166 (2001). doi:10.1021/ja0059084
113. M.S. Gudiksen, C.M. Lieber, Diameter-selective synthesis of semiconductor nanowires J. Am. Chem. Soc. **122**, 8801–8802 (2000). doi:10.1021/ja002008e
114. Z.W. Pan, Z.R. Dai, Z.L. Wang, Nanobelts of semiconducting oxides Science **291**, 1947–1949 (2001). doi:10.1126/science.1058120
115. R.-Q. Zhang, Y. Lifshitz, S.-T. Lee, Oxide-assisted growth of semiconducting nanowires Adv. Mater. **15**, 635–640 (2003). doi:10.1002/adma.200301641
116. Z.R. Dai, Z.W. Pan, Z.L. Wang, Novel nanostructures of functional oxides synthesized by thermal evaporation Adv. Funct. Mater **13**, 9–24 (2003). doi:10.1002/adfm.200390013
117. E. Comini, G. Faglia, G. Sberveglieri, Z.W. Pan, Z.L. Wang, Stable and highly sensitive gas sensors based on semiconducting oxide nanobelts Appl. Phys. Lett **81**, 1869–1871 (2002). doi:10.1063/1.1504867
118. E. Comini, G. Faglia, G. Sberveglieri, D. Calestani, L. Zanotti, M. Zha, Tin oxide nanobelts electrical and sensing properties Sens. Actuators B Chem. **111–112**, 2–6 (2005). doi:10.1016/j.snb.2005.06.031
119. A. Maiti, J.A. Rodriguez, M. Law, P. Kung, U.R. McKinney, P. Yang, SnO_2 nanoribbons as NO_2 sensors: Insights from first principles calculations Nano Lett. **3**, 1025–1028 (2003). doi:10.1021/nl034235v
120. C. Yu, Q. Qing Hao, S. Saha, L. Shi, X. Kong, Z. Wang, Integration of metal oxide nanobelts with microsystems for nerve agent detection Appl. Phys. Lett **86**, 063101 (2005). doi:10.1063/1.1861133
121. D. Meier, S. Semancik, B. Button, E. Strelcov, A. Kolmakov, Coupling nanowire chemiresistors with MEMS microhotplate gas sensing platforms Appl. Phys. Lett **91**, 063118 (2007). doi:10.1063/1.2768861
122. D. Zhang, Z. Liu, C. Li, T. Tang, X. Liu, S. Han, B. Lei, C. Zhou, Detection of NO_2 down to ppb levels using individual and multiple In_2O_3 nanowire devices Nano Lett **4**, 1919–1924 (2004). doi:10.1021/nl0489283
123. V.V. Sysoev, B.K. Button, K. Wepsiec, S. Dmitriev, A. Kolmakov, Toward the nanoscopic "electronic nose": Hydrogen vs carbon monoxide discrimination with an array of individual metal oxide nano- and mesowire sensors Nano Lett **6**, 1584–1588 (2006). doi:10.1021/nl060185t

124. S. Yoo, S.A. Akbar, K.H. Sandhage, Nanocarving of titania (TiO_2): a novel approach for fabricating chemical sensing platform Ceram. Int **30**, 1121–1126 (2004). doi:10.1016/j.ceramint.2003.12.085
125. C. Carney, S. Yoo, S.A. Akbar, TiO_2–SnO_2 nanostructures and their H_2 sensing behavior Sens. Actuators B Chem **108**, 29–33 (2006)
126. A.M. Azad, S.A. Akbar, Novel Structural Modulation in Ceramic Sensors Via Redox Processing in Gas Buffers Int. J. Appl. Ceram. Technol **3**, 177–192 (2006). doi:10.1111/j.1744-7402.2006.02076.x
127. H. Miyazaki, T. Hyodo, Y. Shimizu, M. Egashira, Hydrogen-sensing properties of anodically oxidized TiO_2 film sensors—Effects of preparation and pretreatment conditions Sens. Actuators B Chem **108**, 467–472 (2005). doi:10.1016/j.snb.2004.10.056
128. H.E. Prakasam, K. Shankar, M. Paulose, O.K. Varghese, C.A. Grimes, New Benchmark for TiO2 Nanotube Array Growth by Anodization J. Phys. Chem. C **111**, 7235–7241 (2007). doi:10.1021/jp070273h
129. G.K. Mor, O.K. Varghese, M. Paulose, K.G. Ong, C.A. Grimes, Fabrication of hydrogen sensors with transparent titanium oxide nanotube array thin films as sensing elements Thin Solid Films **496**, 42–48 (2006). doi:10.1016/j.tsf.2005.08.190
130. O.K. Varghese, D. Gong, M. Paulose, K.G. Ong, C.A. Grimes, Hydrogen sensing using titania nanotubes Sens. Actuators B Chem **93**, 338–344 (2003). doi:10.1016/S0925-4005(03)00222-3
131. A. Jaworek, Electrospray droplet sources for thin film deposition J. Mater. Sci **42**, 266–297 (2007). doi:10.1007/s10853-006-0842-9
132. Y. Matsushima, Y. Nemoto, T. Yamazaki, K. Maeda, T. Suzuki, Fabrication of SnO_2 particle-layer on the glass substrate using electrospray pyrolysis method and the gas sensitivity for H_2 Sens. Actuators B Chem **96**, 133–138 (2003). doi:10.1016/S0925-4005(03)00514-8
133. C. Ghimbeu, R. van Landschoot, J. Schoonman, M. Lumbreras, Tungsten trioxide thin films prepared by electrostatic spray deposition technique Thin Solid Films **515**, 5498–5504 (2007). doi:10.1016/j.tsf.2007.01.014
134. D.H. Reneker, I. Chun, Nanometre diameter fibres of polymer, produced by electrospinning Nanotechnology **7**, 216–223 (1996). doi:10.1088/0957-4484/7/3/009
135. I. Kim, A. Rothschild, B.H. Lee, D.Y. Lim, S.M. Jo, H.L. Tuller, Ultrasensitive chemiresistors based on electrospun TiO_2 nanofibres Nano Lett **6**, 2009–2013 (2006). doi:10.1021/nl061197h
136. Y. Dzenis, Spinning continuous fibers for nanotechnology Science **304**, 1917–1919 (2004). doi:10.1126/science.1099074
137. C. Drew, X. Liu, D. Ziegler, X. Wang, F.F. Bruno, J. Whitten, L. A. Samuelson, J. Kumar, Metal oxide-coated polymer nanofibers Nano Lett. **3**, 143–147 (2003). doi:10.1021/nl025850m
138. D. Li, Y. Xia, Fabrication of titania nanofibers by electrospinning Nano Lett **3**, 555–560 (2003). doi:10.1021/nl034039o
139. Z. Liu, D.D. Sun, P. Guo, J. Leckie, An Efficient Bicomponent TiO_2/SnO_2 Nanofiber Photocatalyst Fabricated by Electrospinning with a Side-by-Side Dual Spinneret Method Nano Lett **7**, 1081–1085 (2007). doi:10.1021/nl061898e
140. M.C. Carotta, S. Gherardi, V. Guidi, C. Malagu, G. Martinelli, B. Vendemiati, M. Sacerdoti, G. Ghiotti, S. Morandi, A. Bismuto, P. Maddalena, A. Setaro, (Ti, Sn)O_2 binary solid solutions for gas sensing: Spectroscopic, optical and transport properties Sens. Actuators B Chem. **130**, 38–45 (2008). doi:10.1016/j.snb.2007.07.112
141. K. Sahner, P. Gouma, R. Moos, Electrodeposited and sol–gel precipitated p-type $SrTi_{1-x}Fe_xO_{3-\delta}$ semiconductors for gas sensing. Sensors **7**, 1871–1886 (2007)